

CHARACTERISTIC SWEEPS AND SOURCE ITERATION FOR CHARGED-PARTICLE TRANSPORT WITH CONTINUOUS SLOWING-DOWN AND ANGULAR SCATTERING

BEN S. ASHBY, ALEX LUKYANOV, AND TRISTAN PRYER

ABSTRACT. We develop a semi-analytic deterministic framework for charged-particle transport with continuous slowing-down in energy and angular scattering. Directed transport and energy advection are treated by method-of-characteristics integration, yielding explicit directional sweeps defined by characteristic maps and inflow data. Scattering is incorporated through a fixed-point (source-iteration) scheme in which the angular gain is lagged, yielding a sequence of decoupled directional solves coupled only through angular sums.

The method is formulated variationally in a transport graph space adapted to the charged particle drift. Under standard monotonicity and positivity assumptions on the stopping power and boundedness assumptions on cross sections, we establish coercivity and boundedness of the transport bilinear form, prove contraction of the source iteration under a subcriticality condition and derive a rigorous a posteriori bound for the iteration error, providing an efficient stopping criterion.

We further analyse an elastic discrete-ordinates approximation, including conservation properties and a decomposition of angular error into quadrature, cone truncation and finite iteration effects. Numerical experiments for proton transport validate the characteristic sweep against an exact ballistic benchmark and demonstrate the predicted fixed-point convergence under forward-peaked scattering. Carbon-ion simulations with tabulated stopping powers and a reduced multi-species coupling illustrate Bragg peak localisation and distal tail formation driven by secondary charged fragments.

1. INTRODUCTION

Charged-particle beam therapies (protons, carbon ions) and radiation physics are naturally described by a Boltzmann transport equation (BTE) in position, direction and energy, coupling continuous slowing-down with angular scattering in tissue. In therapy-relevant regimes this produces two numerical challenges: strong anisotropy in angle and a depth-localised Bragg peak generated by energy loss. Efficient deterministic solvers with quantitative stability and error control are therefore attractive when repeated forward solves are required, for example in optimisation, robustness assessment or uncertainty studies [36, 38]. At the microscopic level, the dominant mechanisms can be grouped as ionisation losses, elastic angular deflections and rarer nonelastic nuclear events. Figure 1 shows these schematically for a proton (with analogous mechanisms for heavier ions).

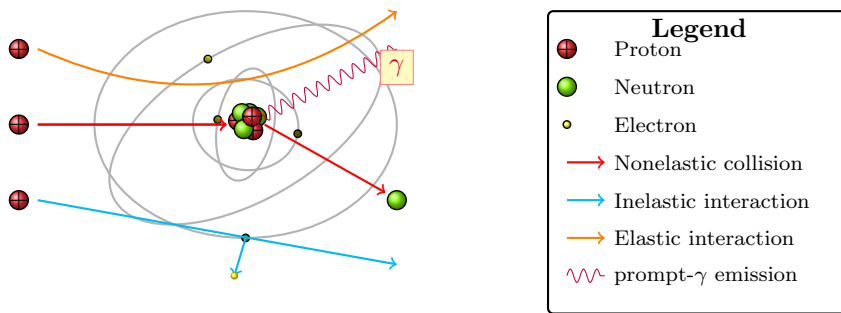


FIGURE 1. *The three main interactions of a proton with matter. A nonelastic proton-nucleus collision, an inelastic Coulomb interaction with atomic electrons and elastic Coulomb scattering with the nucleus.*

Monte Carlo simulation remains the reference approach for high-fidelity charged-particle transport, but its cost can be prohibitive when many forward solves are required [26]. Deterministic methods (discrete-ordinates, moment and pencil-beam-type schemes) offer the prospect of faster, reproducible solves, yet they must address the high dimensionality of phase space and the strong coupling between energy loss and scattering [36, 38]. Recent semi-analytic deterministic solvers show that characteristic integration of continuous slowing-down can deliver fast, reproducible proton transport in regimes where ionisation dominates [4]. A key open difficulty is to retain the same computational advantages while treating angular redistribution explicitly and with quantitative control of the scattering coupling.

We present a semi-analytic method-of-characteristics (MoC) framework for charged-particle transport with continuous slowing-down in energy and angular scattering. Directed transport and energy advection are handled by characteristic integration, so each directional sweep amounts to evaluating an explicit characteristic map together with the prescribed inflow data. Scattering is included through a source-iteration (fixed-point) strategy in which the angular gain is lagged, so that each iteration requires only a collection of direction-by-direction sweeps coupled through angular sums. This preserves the sweep structure of ionisation-only characteristic solvers while adding scattering through an iterative angular mixing step.

We place the method in a variational setting based on a graph space adapted to the directional and energy drift. Under monotonicity and positivity assumptions on the stopping power and boundedness assumptions on the cross sections, we establish coercivity and boundedness of the transport bilinear form and obtain well-posedness of the weak problem. These stability results support convergence of the source iteration and yield rigorous a posteriori bounds for the iteration error, giving a practical stopping criterion. For the discrete-ordinates approximation we further decompose the angular error into contributions from angular quadrature, cone truncation and the finite iteration count.

We implement the framework for proton transport with Bragg–Kleeman-type stopping and for carbon-ion transport using tabulated stopping powers. In the carbon case we include a reduced multi-species construction in which a secondary proton and neutron field is generated by a volumetric source driven by the converged carbon solution and an effective interaction rate, to provide a transparent mechanism for post-peak dose tails and to validate the coupling logic. Numerical experiments verify the characteristic solver against an analytic benchmark, demonstrate linear convergence of the source iteration and illustrate the impact of forward-peaked scattering and the multi-species coupling on depth–dose, including the distal secondary tail in the carbon simulations.

Charged-particle transport spans rigorous kinetic theory, high-fidelity stochastic simulation and fast deterministic or surrogate algorithms. Foundational treatments of the linear Boltzmann equation and of transport operators provide the analytical setting for scattering kernels, conservation, boundary conditions and angular representations [11, 28, 32, 37]. Reliable stopping-power and range–energy data underpin dose prediction across modalities; recommended datasets and reviews document proton and heavy-ion stopping powers, dosimetry constants and corrections beyond simple power laws [7, 8, 33, 34, 35]. Against this backdrop, high dimensionality (space, direction, energy), strongly forward-peaked scattering and continuous slowing-down combine to make full BTE solutions challenging in therapy-relevant geometries and materials.

Monte Carlo remains the reference approach for transport with detailed physics and is widely implemented in general-purpose toolkits and transport libraries [2, 20, 29]. Clinical dose calculation has benefited from proton-specific MC implementations and accelerations tailored to voxelised media and beam modelling [19]. Despite these advances, computational expense can limit throughput in planning and uncertainty studies and surveys of grid-based and MC algorithms emphasise the trade-off between fidelity and speed in clinical settings [26].

Deterministic discretisations provide complementary capabilities. Discrete-ordinates (S_N) and spherical-harmonics (P_N/SP_N) methods discretise or expand the angular dependence and are extensively reviewed for nuclear and radiation applications, including stability considerations for strongly anisotropic scattering [38]. Pencil-beam and Fokker–Planck reductions offer further simplification for forward-peaked beams and accuracy analyses quantify regimes where such approximations capture the parent BTE and where they break down, for example under large-angle scatter or in heterogeneous media [9]. Algorithmically, fast beam models for therapy incorporate upstream devices and air gaps and remain influential for treatment planning workflows [22]. In therapy settings, forward-peaked scattering is often represented through simple

parametric phase functions such as the Henyey–Greenstein kernel [21], which provides a convenient testbed for discrete–ordinates and iterative scattering solvers.

Recent developments aim to improve scalability and structure preservation for charged–particle transport. Dynamical low–rank formulations reduce angular–energy complexity by evolving a factored representation with collided/uncollided splitting, providing deterministic alternatives to full S_N in high dimensions [36]. Positivity–preserving finite element frameworks enforce nonnegativity and conservation in deterministic dose computation, improving robustness in heterogeneous media and complex geometries [3]. Efficient analytic or semi–analytic solvers have been derived for proton transport by combining characteristic integration of the slowing–down term with tractable scattering closures [4]. High–order space–angle–energy discontinuous Galerkin formulations on polytopic meshes provide a route to accurate deterministic Boltzmann solves on complex geometries [24]. The resulting large coupled linear systems motivate scalable iterative solvers and computable a posteriori algebraic error control [23]. For sweeping on complex meshes, cycle–free strategies on polytopal grids enable DG–style discretisations with guaranteed orderings, extending transport solvers beyond structured meshes [10, 18].

There is parallel progress in modelling, inversion and uncertainty. A unified operator–theoretic perspective links transport descriptions to planning objectives and controls, clarifying the interface between forward models, adjoints and optimisation in proton therapy [27]. Stochastic differential equation formulations provide mesoscopic descriptions with structure–preserving discretisations encoding geometry, energy loss, angular diffusion and sensitivity [16, 17, 14]. Data–driven surrogates with uncertainty quantification offer rapid dose emulation with quantified predictive spread [31]. Bayesian inverse formulations demonstrate how prompt gamma or related signals can be used to verify delivered dose fields, integrating transport models with statistical inference for on–line quality assurance [15].

The semi–analytic approach developed here sits between high–fidelity MC transport and heavily reduced beam models. It retains an explicit angular description of scattering while exploiting characteristic integration of continuous slowing–down in energy and it is designed to interface naturally with conservation–aware discretisations and with uncertainty or inverse formulations. This positioning is consistent with the classical transport literature [11, 28, 32, 37], the data foundations for stopping power and dosimetry [7, 8, 33, 34, 35], and contemporary advances in scalable deterministic and hybrid transport algorithms [38, 36, 4, 3, 10], with practical relevance for treatment planning and verification. From a numerical–transport perspective, the present work also draws on classical analyses of inflow trace spaces for kinetic transport [12, 13] and on the extensive literature on source iteration and its convergence properties in discrete ordinates transport [1, 30].

The rest of the paper is set out as follows. In §2 we introduce the charged–particle transport models considered in this work, define the phase–space setting and specify the scattering and slowing–down structure that motivates the subsequent analysis. In §3 we derive a variational formulation in an appropriate graph space, establish coercivity and boundedness of the continuous transport bilinear form and prove convergence of the continuum source iteration. In §4 we develop the discrete–ordinates angular approximation and discuss conservation properties of the discrete scattering operator. In §5 we give error control that separates angular quadrature, cone truncation and iteration effects. In §6 we present numerical experiments for proton transport, including an exact benchmark for the ballistic limit, convergence tests for the source iteration and simulations with Henyey–Greenstein scattering. In §7 we extend the implementation to carbon ions using tabulated stopping powers and a reduced multi–species construction generating secondary protons and neutrons, and we illustrate the resulting depth–dose behaviour including distal tail formation beyond the primary carbon peak.

2. CHARGED PARTICLE TRANSPORT MODELS

We consider transport of charged particles through a medium, governed by directed motion, ionising energy loss and scattering due to elastic and nonelastic interactions. Let $D \subset \mathbb{R}^d$ with $d \in \{2, 3\}$ denote the spatial domain, and let $I = [E_{\min}, E_{\max}] \subset (0, \infty)$ be the admissible energy interval. The phase-space domain is $\Omega = D \times I \times \mathbb{S}^{d-1}$, where $\omega \in \mathbb{S}^{d-1}$ is the unit direction of travel. The surface measure on \mathbb{S}^{d-1} is denoted $d\omega$.

For a given particle species, the phase-space density $\psi(x, E, \omega)$ satisfies the linear Boltzmann transport equation

$$(1) \quad \omega \cdot \nabla_x \psi(x, E, \omega) + \sigma_T(E) \psi(x, E, \omega) = \mathcal{K}[\psi](x, E, \omega),$$

where $\sigma_T(E) \geq 0$ is the total removal cross-section and \mathcal{K} is the gain operator

$$(2) \quad \mathcal{K}[\psi](x, E, \omega) := \int_{\mathbb{S}^{d-1}} \int_I \sigma_S(\omega, \omega', E' \rightarrow E) \psi(x, E', \omega') dE' d\omega'.$$

The differential kernel $\sigma_S \geq 0$ redistributes particles from (E', ω') to (E, ω) . The quantity $\sigma_T(E)$ is taken as given so that the loss term $\sigma_T(E)\psi$ controls \mathcal{K} in the energy norm introduced later.

The kernel σ_S contains distinct physical mechanisms. We write

$$(3) \quad \sigma_S(\omega, \omega', E' \rightarrow E) = \sigma_{\text{el}}(\omega, \omega', E) \delta(E - E') + \sigma_{\text{ion}}(\omega, \omega', E' \rightarrow E) + \sigma_{\text{non}}(\omega, \omega', E' \rightarrow E),$$

where σ_{el} models elastic Coulomb scattering, which is energy-conserving, σ_{ion} models ionisation losses and σ_{non} models genuinely nonelastic interactions that can involve larger energy transfers.

In the energy regime of interest here, ionisation energy loss arises from a large number of inelastic collisions along each particle track, with each collision typically transferring only a small amount of energy. In this setting it is standard to replace the detailed ionisation energy-loss redistribution by a continuous slowing-down approximation, in which the cumulative effect of ionisation is represented by an energy advection term with stopping power $S(E)$. Neglecting higher-order energy-diffusion (straggling) corrections, this leads to the charged-particle transport model

$$(4) \quad \omega \cdot \nabla_x \psi(x, E, \omega) - \partial_E(S(E)\psi(x, E, \omega)) + \sigma_T(E)\psi(x, E, \omega) = \mathcal{K}[\psi](x, E, \omega),$$

where, after applying the slowing down approximation, \mathcal{K} collects the remaining gain contributions, including elastic angular redistribution and any nonelastic energy-changing events retained in the model.

In regimes where small-angle Coulomb scattering dominates, the elastic gain can be approximated by angular diffusion on the sphere via the Laplace–Beltrami operator Δ_ω ,

$$(5) \quad \int_{\mathbb{S}^{d-1}} \sigma_{\text{el}}(\omega, \omega', E) \psi(x, E, \omega') d\omega' \approx \varepsilon(E) \Delta_\omega \psi(x, E, \omega),$$

with $\varepsilon(E) \geq 0$ an energy-dependent angular-diffusion coefficient [3].

Throughout the analysis we adopt the following regularity and positivity conditions, consistent with the variational framework developed later: $S \in W^{1,\infty}(I)$ with $S(E) > 0$ and $S'(E) \leq 0$ on I , $\sigma_T \in L^\infty(I)$ with $\sigma_T(E) \geq 0$, and $\sigma_S \in L^\infty(\mathbb{S}^{d-1} \times \mathbb{S}^{d-1} \times I \times I)$ with $\sigma_S \geq 0$. These ensure that the gain operator (2) is bounded on the graph space used for the weak formulation and that the transport part of (4) is coercive once inflow boundary conditions are imposed.

2.1. Stopping power and the Bragg–Kleeman approximation. Under the continuous slowing down approximation, ionisation losses are represented in (4) by the stopping power $S(E)$. For light ions such as protons the dominant mechanism is electronic stopping due to Coulomb interactions with atomic electrons. A standard empirical model is the Bragg–Kleeman rule: given constants $\alpha > 0$ and $p \in [1, 2]$,

$$(6) \quad S(E) = \frac{1}{\alpha p} E^{1-p}.$$

This follows from the range–energy relation $R(E) = \alpha E^p$ and is well validated in the therapeutic window for protons. In particular, on any admissible interval $I = [E_{\min}, E_{\max}] \subset (0, \infty)$ one has $S \in W^{1,\infty}(I)$, $S(E) > 0$ and $S'(E) \leq 0$, properties used below to obtain coercivity of the transport operator. One can see in Figure 2 how this ansatz is very accurate for clinically relevant proton energies since ionisation dominates nonelastic processes.

A more physically motivated alternative is the Bethe–Bloch formula for the electronic stopping power, which models the mean ionisation loss in terms of projectile speed and material parameters. It provides a standard reference across ion species and, with suitable effective parameters, can be used as an accurate surrogate for electronic stopping in the therapeutic energy range. In the present work we do not pursue a full Bethe–Bloch parameterisation and instead adopt the Bragg–Kleeman approximation (6) as the simplest closed-form model that is sufficient for our analysis and numerical examples.

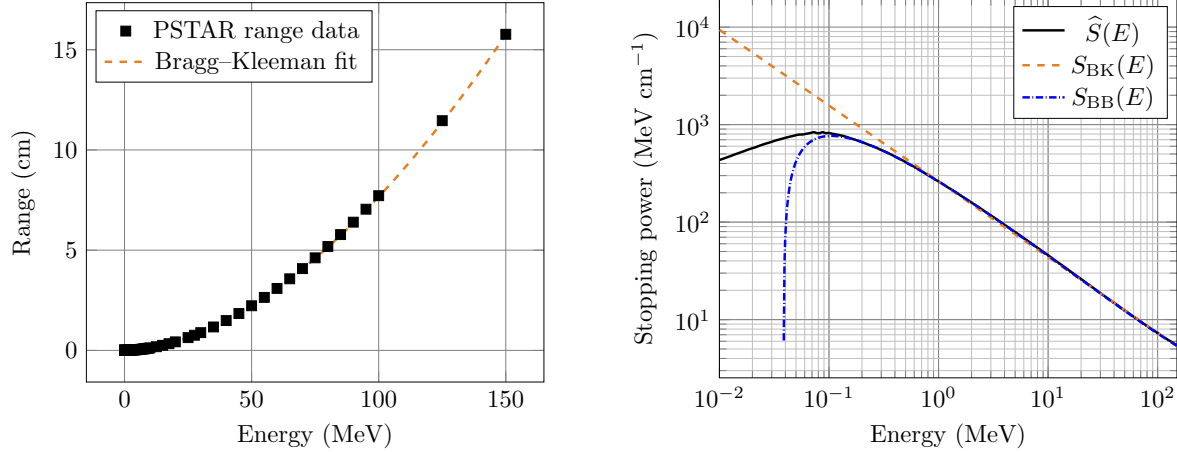


FIGURE 2. Left: proton range–energy data in water from PSTAR with Bragg–Kleeman fit $R_{BK}(E) = \alpha E^p$. Right: stopping power reconstructed from the same range data via $\hat{S}(E) = (dR/dE)^{-1}$, obtained by differentiating a cubic spline fit of $R(E)$, together with the Bragg–Kleeman stopping power $S_{BK}(E) = (\alpha p E^{p-1})^{-1}$ and a Bethe–Bloch stopping power $S_{BB}(E)$. Data taken from PSTAR [6].

2.2. Data-informed stopping for heavy ions. For heavier ions, nuclear and other nonelastic processes become non-negligible as energy decreases, leading to systematic deviations from the Bragg–Kleeman form (6). These deviations are not remedied by changing the electronic stopping model alone (for example by switching to a Bethe–Bloch form), since they reflect genuinely nonelastic contributions to the total stopping in the slowing-down regime. As can be seen in Figure 3 for carbon ions this effect is evident at low energies, reflecting fragmentation and secondary production. In this regime we take $S(E)$ to be a data-informed stopping power obtained directly from range–energy and stopping data, rather than enforcing the parametric form (6).

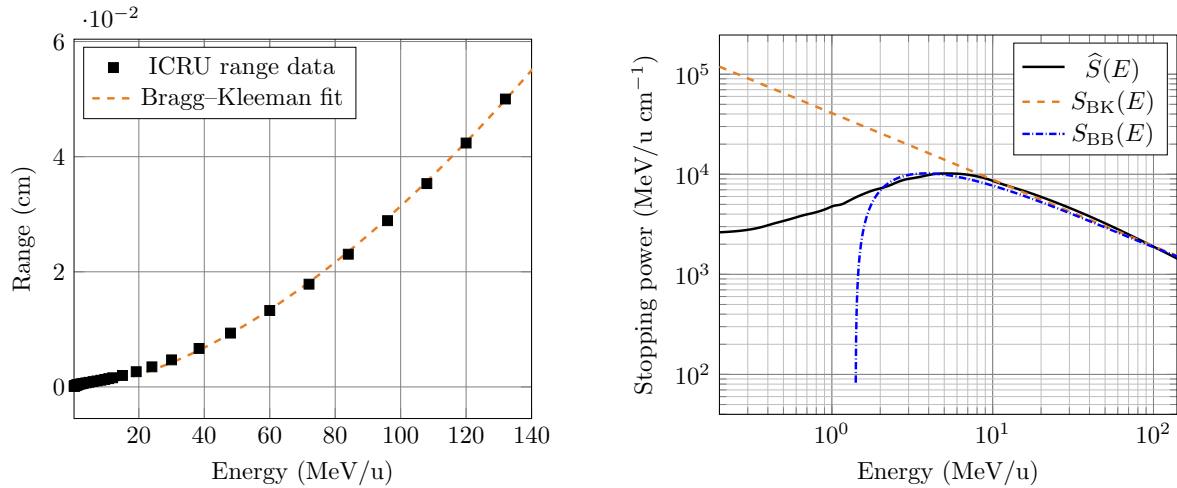


FIGURE 3. Left: carbon range–energy data from ICRU with Bragg–Kleeman fit $R_{BK}(E) = \alpha E^p$ (energy in MeV/u). Right: stopping power reconstructed from the same range data via $\hat{S}(E) = (dR/dE)^{-1}$, obtained by differentiating a cubic spline fit of $R(E)$, together with the Bragg–Kleeman stopping power $S_{BK}(E) = (\alpha p E^{p-1})^{-1}$ and a Bethe–Bloch-shaped surrogate $S_{BB}(E)$. Data taken from ICRU [25].

For the analysis we work on an interval $I = [E_{\min}, E_{\max}]$ bounded away from 0 and assume that the fitted S satisfies $S \in W^{1,\infty}(I)$, $S(E) > 0$ and $S'(E) \leq 0$ on I . In practice this is achieved by using a smooth monotone fit of the tabulated data over the energies of interest.

2.3. Boundary conditions. Since $S(E) > 0$ on I , the energy drift term $-\partial_E(S\psi)$ induces a one-way characteristic flow from E_{\max} down to E_{\min} . It is therefore natural to prescribe data both on the spatial inflow boundary and on the top-energy boundary.

Let $\partial(D \times I) = (\partial D \times I) \cup (D \times \partial I)$ and write the outward unit normal on $\partial(D \times I)$ as $\mathbf{n}_{(\mathbf{x}, E)} := (\mathbf{n}_{\mathbf{x}}, n_E)$, where $\mathbf{n}_{\mathbf{x}}$ is the outward unit normal on ∂D , and $n_E = +1$ on $E = E_{\max}$ and $n_E = -1$ on $E = E_{\min}$. For each fixed $\omega \in \mathbb{S}^{d-1}$ we define the inflow and outflow boundaries in (\mathbf{x}, E) by

$$\Gamma_{\pm}(\omega) := \{(\mathbf{x}, E) \in \partial(D \times I) : \pm(\omega \cdot \mathbf{n}_{\mathbf{x}} - S(E)n_E) > 0\},$$

and the corresponding phase-space boundary sets by

$$\Gamma_{\pm} := \{(\mathbf{x}, E, \omega) \in \partial(D \times I) \times \mathbb{S}^{d-1} : (\mathbf{x}, E) \in \Gamma_{\pm}(\omega)\}.$$

This recovers the usual decomposition into spatial and energy inflow/outflow. On the spatial boundary $\partial D \times I$ one has $n_E = 0$, so

$$\Gamma_{-}^{\omega} := \{(\mathbf{x}, E, \omega) \in (\partial D \times I) \times \mathbb{S}^{d-1} : \omega \cdot \mathbf{n}_{\mathbf{x}} < 0\}, \quad \Gamma_{+}^{\omega} := \{(\mathbf{x}, E, \omega) \in (\partial D \times I) \times \mathbb{S}^{d-1} : \omega \cdot \mathbf{n}_{\mathbf{x}} > 0\}.$$

On the energy boundary $D \times \partial I$ one has $\mathbf{n}_{\mathbf{x}} = \mathbf{0}$, so the flux associated with $-\partial_E(S\psi)$ is $-S(E)n_E\psi$. Since $S(E) > 0$, the top boundary $E = E_{\max}$ is inflow and the bottom boundary $E = E_{\min}$ is outflow. We set

$$\Gamma_{-}^E := D \times \{E_{\max}\} \times \mathbb{S}^{d-1}, \quad \Gamma_{+}^E := D \times \{E_{\min}\} \times \mathbb{S}^{d-1},$$

so that

$$\Gamma_{-} = \Gamma_{-}^{\omega} \cup \Gamma_{-}^E, \quad \Gamma_{+} = \Gamma_{+}^{\omega} \cup \Gamma_{+}^E.$$

On Γ_{-} we prescribe inflow data

$$(7) \quad \psi = g \quad \text{on } \Gamma_{-}.$$

We assume g is square-integrable with respect to the natural flux weights induced by the boundary term $\omega \cdot \mathbf{n}_{\mathbf{x}} - S(E)n_E$, namely $|\omega \cdot \mathbf{n}_{\mathbf{x}}|$ on Γ_{-}^{ω} and $S(E_{\max})$ on Γ_{-}^E :

$$g \in L^2(\Gamma_{-}^{\omega}, |\omega \cdot \mathbf{n}_{\mathbf{x}}| d\gamma_{\mathbf{x}} dE d\omega) \cap L^2(\Gamma_{-}^E, S(E_{\max}) d\mathbf{x} d\omega).$$

No boundary condition is imposed on Γ_{+} .

3. VARIATIONAL FORMULATION AND FUNCTIONAL SETTING

To analyse well-posedness and enable discretisation, we adopt a variational formulation. The first-order transport and energy-advection terms, together with the non-symmetric gain operator, motivate a graph space that captures directional and energy drift.

We work in the graph space

$$(8) \quad \mathcal{U} := \left\{ u \in L^2(\Omega) : \omega \cdot \nabla_x u \in L^2(\Omega), \partial_E(S(E)u) \in L^2(\Omega) \right\}.$$

For each fixed $\omega \in \mathbb{S}^{d-1}$, define the directional bilinear form

$$(9) \quad a(u, v; \omega) := \int_D \int_I \left[(\omega \cdot \nabla_x u) v - \partial_E(S(E)u) v + \sigma_T(E)uv \right] dE d\mathbf{x} + \frac{1}{2} \int_{\Gamma_{+}(\omega)} (\omega \cdot \mathbf{n}_{\mathbf{x}} - S(E)n_E) uv ds,$$

and the scattering bilinear form

$$(10) \quad s(u, v; \omega) := \int_D \int_I v(\mathbf{x}, E, \omega) \int_{\mathbb{S}^{d-1}} \int_I \sigma_S(\omega, \omega', E' \rightarrow E) u(\mathbf{x}, E', \omega') dE' d\omega' dE d\mathbf{x}.$$

The linear form is

$$(11) \quad l(v; \omega) := -\frac{1}{2} \int_{\Gamma_{-}(\omega)} (\omega \cdot \mathbf{n}_{\mathbf{x}} - S(E)n_E) g(\mathbf{x}, E, \omega) v(\mathbf{x}, E, \omega) ds + \int_D \int_I f(\mathbf{x}, E, \omega) v(\mathbf{x}, E, \omega) dE d\mathbf{x},$$

where g is the inflow boundary datum on $\Gamma_-(\omega)$ and $f \in L^2(\Omega)$ is a given volumetric source. In the present paper f will be used to represent any modelling corrections or additional physics that are treated explicitly rather than embedded in the drift.

The weak problem reads: find $u \in \mathcal{U}$ such that

$$(12) \quad \int_{\mathbb{S}^{d-1}} a(u, v; \omega) d\omega = \int_{\mathbb{S}^{d-1}} [s(u, v; \omega) + l(v; \omega)] d\omega \quad \text{for all } v \in \mathcal{U}.$$

In the stability and contraction arguments below we apply the coercivity estimate to functions with homogeneous inflow trace on Γ_- (in particular to source-iteration differences, for which the inflow datum cancels since g is fixed in l).

3.1. Theorem (Coercivity and boundedness of the continuous bilinear forms). *Assume $S \in W^{1,\infty}(I)$ with $S(E) > 0$ and $S'(E) \leq 0$ on I , $\sigma_T \in L^\infty(I)$ with $\sigma_T(E) \geq 0$, and $\sigma_S \in L^\infty(\mathbb{S}^{d-1} \times \mathbb{S}^{d-1} \times I \times I)$ with $\sigma_S \geq 0$.*

Define the coercivity norm

$$\|u\|_{\mathcal{U}}^2 := \|\sigma_T^{1/2} u\|_{L^2(\Omega)}^2 + \|(-S'(E))^{1/2} u\|_{L^2(\Omega)}^2 + \int_{\Gamma_+} (\omega \cdot \mathbf{n}_x - S(E) n_E) u^2 ds,$$

and the stronger norm

$$\|u\|_{\mathcal{U}^*}^2 := \|u\|_{\mathcal{U}}^2 + \|\nabla_x u\|_{L^2(\Omega)}^2 + \|\partial_E u\|_{L^2(\Omega)}^2.$$

Assume moreover that

$$\mu := \text{ess inf}_{E \in I} (-S'(E)) > 0,$$

so that $\|w\|_{L^2(\Omega)} \leq \mu^{-1/2} \|(-S')^{1/2} w\|_{L^2(\Omega)} \leq \mu^{-1/2} \|w\|_{\mathcal{U}}$.

Then the bilinear forms $a(u, v; \omega)$ and $s(u, v; \omega)$ defined in Section 3 satisfy the following:

(1) *Coercivity. If $u = 0$ on Γ_- , then*

$$\int_{\mathbb{S}^{d-1}} a(u, u; \omega) d\omega \geq \frac{1}{2} \|u\|_{\mathcal{U}}^2.$$

(2) *Boundedness. There exists $C_a > 0$, depending only on $\|S\|_{W^{1,\infty}(I)}$, $\|\sigma_T\|_{L^\infty(I)}$ and μ , such that for all $u \in \mathcal{U}^*$ and all $v \in \mathcal{U}$,*

$$\left| \int_{\mathbb{S}^{d-1}} a(u, v; \omega) d\omega \right| \leq C_a \|u\|_{\mathcal{U}^*} \|v\|_{\mathcal{U}}.$$

Moreover there exists $C_s > 0$, depending only on $\|\sigma_S\|_{L^\infty}$ and the measures of I and \mathbb{S}^{d-1} , such that

$$\left| \int_{\mathbb{S}^{d-1}} s(u, v; \omega) d\omega \right| \leq C_s \|u\|_{L^2(\Omega)} \|v\|_{L^2(\Omega)} \leq C_s \mu^{-1} \|u\|_{\mathcal{U}} \|v\|_{\mathcal{U}}.$$

Proof. Fix $\omega \in \mathbb{S}^{d-1}$ and abbreviate $a(u, u) := a(u, u; \omega)$. By definition,

$$a(u, u) = \int_D \int_I [(\omega \cdot \nabla_x u) u - \partial_E(Su) u + \sigma_T u^2] dE dx + \frac{1}{2} \int_{\Gamma_+(\omega)} (\omega \cdot \mathbf{n}_x - S n_E) u^2 d\gamma.$$

We first integrate by parts in x . Since $(\omega \cdot \nabla_x u) u = \frac{1}{2} \omega \cdot \nabla_x (u^2)$,

$$\int_D \int_I (\omega \cdot \nabla_x u) u dE dx = \frac{1}{2} \int_{\partial D \times I} (\omega \cdot \mathbf{n}_x) u^2 d\gamma.$$

For the energy-advection term, write

$$-\partial_E(Su) u = -\frac{1}{2} \partial_E(Su^2) + \frac{1}{2} (-S') u^2,$$

so that integration by parts in E gives

$$-\int_D \int_I \partial_E(Su) u dE dx = -\frac{1}{2} \int_{D \times \partial I} S n_E u^2 d\gamma + \frac{1}{2} \int_D \int_I (-S'(E)) u^2 dE dx.$$

Combining the x and E boundary contributions yields

$$\frac{1}{2} \int_{\partial(D \times I)} (\omega \cdot \mathbf{n}_x - S n_E) u^2 d\gamma = \frac{1}{2} \int_{\Gamma_+(\omega)} (\omega \cdot \mathbf{n}_x - S n_E) u^2 d\gamma + \frac{1}{2} \int_{\Gamma_-(\omega)} (\omega \cdot \mathbf{n}_x - S n_E) u^2 d\gamma.$$

Therefore

$$\begin{aligned} a(u, u) &= \|\sigma_T^{1/2} u(\cdot, \cdot, \omega)\|_{L^2(D \times I)}^2 + \frac{1}{2} \|(-S')^{1/2} u(\cdot, \cdot, \omega)\|_{L^2(D \times I)}^2 \\ &\quad + \int_{\Gamma_+(\omega)} (\omega \cdot \mathbf{n}_x - S n_E) u^2 d\gamma + \frac{1}{2} \int_{\Gamma_-(\omega)} (\omega \cdot \mathbf{n}_x - S n_E) u^2 d\gamma. \end{aligned}$$

If $u = 0$ on Γ_- , then for each fixed ω we have $u = 0$ on $\Gamma_-(\omega)$ and the last term vanishes. Hence

$$a(u, u) \geq \frac{1}{2} \|\sigma_T^{1/2} u(\cdot, \cdot, \omega)\|_{L^2(D \times I)}^2 + \frac{1}{2} \|(-S')^{1/2} u(\cdot, \cdot, \omega)\|_{L^2(D \times I)}^2 + \frac{1}{2} \int_{\Gamma_+(\omega)} (\omega \cdot \mathbf{n}_x - S n_E) u^2 d\gamma.$$

Integrating this inequality over \mathbb{S}^{d-1} and using $ds = d\gamma d\omega$ gives

$$\int_{\mathbb{S}^{d-1}} a(u, u; \omega) d\omega \geq \frac{1}{2} \|\sigma_T^{1/2} u\|_{L^2(\Omega)}^2 + \frac{1}{2} \|(-S')^{1/2} u\|_{L^2(\Omega)}^2 + \frac{1}{2} \int_{\Gamma_+} (\omega \cdot \mathbf{n}_x - S n_E) u^2 ds = \frac{1}{2} \|u\|_{\mathcal{U}}^2,$$

which proves coercivity.

For boundedness of a , fix ω and apply Cauchy–Schwarz, together with

$$\|\partial_E(Su)\|_{L^2(\Omega)} \leq \|S\|_{L^\infty(I)} \|\partial_E u\|_{L^2(\Omega)} + \|S'\|_{L^\infty(I)} \|u\|_{L^2(\Omega)}$$

we have

$$\begin{aligned} \left| \int_D \int_I (\omega \cdot \nabla_x u) v \right| &\leq \|\nabla_x u(\cdot, \cdot, \omega)\|_{L^2(D \times I)} \|v(\cdot, \cdot, \omega)\|_{L^2(D \times I)}, \\ \left| \int_D \int_I \partial_E(Su) v \right| &\leq \|\partial_E(Su)(\cdot, \cdot, \omega)\|_{L^2(D \times I)} \|v(\cdot, \cdot, \omega)\|_{L^2(D \times I)} \\ &\leq \|S\|_{W^{1,\infty}(I)} (\|\partial_E u(\cdot, \cdot, \omega)\|_{L^2(D \times I)} + \|u(\cdot, \cdot, \omega)\|_{L^2(D \times I)}) \|v(\cdot, \cdot, \omega)\|_{L^2(D \times I)}, \\ \left| \int_D \int_I \sigma_T u v \right| &\leq \|\sigma_T\|_{L^\infty(I)} \|u(\cdot, \cdot, \omega)\|_{L^2(D \times I)} \|v(\cdot, \cdot, \omega)\|_{L^2(D \times I)}, \\ \left| \frac{1}{2} \int_{\Gamma_+(\omega)} (\omega \cdot \mathbf{n}_x - S n_E) u v d\gamma \right| &\leq \frac{1}{2} \left(\int_{\Gamma_+(\omega)} (\omega \cdot \mathbf{n}_x - S n_E) u^2 d\gamma \right)^{1/2} \left(\int_{\Gamma_+(\omega)} (\omega \cdot \mathbf{n}_x - S n_E) v^2 d\gamma \right)^{1/2}. \end{aligned}$$

Using $\|w\|_{L^2(\Omega)} \leq \mu^{-1/2} \|w\|_{\mathcal{U}}$ for $w = v$ and $\|u\|_{L^2(\Omega)} \leq \mu^{-1/2} \|u\|_{\mathcal{U}} \leq \mu^{-1/2} \|u\|_{\mathcal{U}^*}$, we obtain a bound of the form $|a(u, v; \omega)| \leq C_a \|u\|_{\mathcal{U}^*} \|v\|_{\mathcal{U}}$ with C_a independent of ω . Integrating over \mathbb{S}^{d-1} yields the stated estimate.

For the scattering form, define

$$\mathcal{K}[u](\mathbf{x}, E, \omega) := \int_{\mathbb{S}^{d-1}} \int_I \sigma_S(\omega, \omega', E' \rightarrow E) u(\mathbf{x}, E', \omega') dE' d\omega'.$$

By Fubini and $\|\sigma_S\|_{L^\infty} < \infty$,

$$|\mathcal{K}[u](\mathbf{x}, E, \omega)| \leq \|\sigma_S\|_{L^\infty} \int_{\mathbb{S}^{d-1}} \int_I |u(\mathbf{x}, E', \omega')| dE' d\omega'.$$

Applying Cauchy–Schwarz in (E', ω') gives

$$|\mathcal{K}[u](\mathbf{x}, E, \omega)| \leq \|\sigma_S\|_{L^\infty} (|I| |\mathbb{S}^{d-1}|)^{1/2} \left(\int_{\mathbb{S}^{d-1}} \int_I |u(\mathbf{x}, E', \omega')|^2 dE' d\omega' \right)^{1/2}.$$

Squaring, integrating over (\mathbf{x}, E, ω) and using Fubini yields $\|\mathcal{K}[u]\|_{L^2(\Omega)} \leq C_s \|u\|_{L^2(\Omega)}$ with C_s depending only on $\|\sigma_S\|_{L^\infty}$ and the measures of I and \mathbb{S}^{d-1} . Hence

$$\left| \int_{\mathbb{S}^{d-1}} s(u, v; \omega) d\omega \right| = \left| \int_{\Omega} v \mathcal{K}[u] \right| \leq \|v\|_{L^2(\Omega)} \|\mathcal{K}[u]\|_{L^2(\Omega)} \leq C_s \|u\|_{L^2(\Omega)} \|v\|_{L^2(\Omega)}.$$

The final inequality in the theorem follows from $\|w\|_{L^2(\Omega)} \leq \mu^{-1/2} \|w\|_{\mathcal{U}}$ for $w = u, v$. \square

3.2. Source iteration at the continuum level. The weak formulation (12) couples all directions through the gain form $s(\cdot, \cdot; \omega)$. To decouple angles and obtain an efficient solver, we employ a (Picard) source iteration in which the gain is lagged. Given an initial guess $u^{(0)} \in \mathcal{U}$, define $\{u^{(n)}\}_{n \geq 1}$ by the following directional problems: for each $\omega \in \mathbb{S}^{d-1}$, find $u^{(n)}(\cdot, \cdot, \omega) \in \mathcal{U}$ such that

$$(13) \quad a(u^{(n)}, v; \omega) = s(u^{(n-1)}, v; \omega) + l(v; \omega) \quad \text{for all } v \in \mathcal{U},$$

where a , s and l are the forms from Section 3. In particular, the inflow boundary datum g is enforced in the linear functional $l(\cdot; \omega)$ and is not updated with n .

3.3. Proposition (Convergence of source iteration). *Assume the hypotheses of Theorem 3.1 and that the gain operator induces a bounded bilinear form on \mathcal{U} in the sense that there exists $\eta \geq 0$ such that*

$$(14) \quad \left| \int_{\mathbb{S}^{d-1}} s(w, v; \omega) \, d\omega \right| \leq \eta \|w\|_{\mathcal{U}} \|v\|_{\mathcal{U}} \quad \text{for all } w, v \in \mathcal{U}.$$

If $2\eta < 1$, then the Picard map induced by (13) is a strict contraction on \mathcal{U} in the $\|\cdot\|_{\mathcal{U}}$ norm. Consequently, for any initial guess $u^{(0)} \in \mathcal{U}$ the iterates $\{u^{(n)}\}_{n \geq 0}$ defined by (13) converge strongly in \mathcal{U} to the unique solution u of the variational problem (12).

In particular, by Theorem 3.1 one may take $\eta = C_s \mu^{-1}$, where C_s is the scattering boundedness constant.

Proof. Define the integrated bilinear forms

$$A(u, v) := \int_{\mathbb{S}^{d-1}} a(u, v; \omega) \, d\omega, \quad S(u, v) := \int_{\mathbb{S}^{d-1}} s(u, v; \omega) \, d\omega,$$

and likewise $L(v) := \int_{\mathbb{S}^{d-1}} l(v; \omega) \, d\omega$. Then the weak problem (12) reads $A(u, v) = S(u, v) + L(v)$ for all $v \in \mathcal{U}$, and the source iteration (13) reads

$$A(u^{(n)}, v) = S(u^{(n-1)}, v) + L(v) \quad \text{for all } v \in \mathcal{U}.$$

Let $T : \mathcal{U} \rightarrow \mathcal{U}$ denote the Picard map defined by $u^{(n)} = T(u^{(n-1)})$, that is, $T(w)$ is the unique element of \mathcal{U} satisfying

$$(15) \quad A(T(w), v) = S(w, v) + L(v) \quad \text{for all } v \in \mathcal{U}.$$

(Existence and uniqueness of $T(w)$ follow from the well-posedness associated with Theorem 3.1; in particular, the boundary datum is fixed in L and is therefore the same for all arguments w .)

To prove contraction, let $w_1, w_2 \in \mathcal{U}$ and set $\delta := T(w_1) - T(w_2)$. Subtracting (15) for w_1 and w_2 gives

$$(16) \quad A(\delta, v) = S(w_1 - w_2, v) \quad \text{for all } v \in \mathcal{U}.$$

Since the inflow datum is fixed in L , it cancels in the difference, and δ has homogeneous inflow trace on Γ_- (equivalently, δ belongs to the homogeneous-inflow subspace used in Theorem 3.1). Choosing $v = \delta$ in (16) and applying the coercivity estimate from Theorem 3.1 yields

$$(17) \quad \frac{1}{2} \|\delta\|_{\mathcal{U}}^2 \leq |S(w_1 - w_2, \delta)|.$$

Using (14) gives

$$\frac{1}{2} \|\delta\|_{\mathcal{U}}^2 \leq \eta \|w_1 - w_2\|_{\mathcal{U}} \|\delta\|_{\mathcal{U}}, \quad \text{hence} \quad \|\delta\|_{\mathcal{U}} \leq 2\eta \|w_1 - w_2\|_{\mathcal{U}}.$$

Therefore $\|T(w_1) - T(w_2)\|_{\mathcal{U}} \leq 2\eta \|w_1 - w_2\|_{\mathcal{U}}$. If $2\eta < 1$, T is a strict contraction on \mathcal{U} . Banach's fixed point theorem implies that $u^{(n)} \rightarrow u$ strongly in \mathcal{U} , where u is the unique fixed point of T , and inserting $u = T(u)$ in (15) shows that u satisfies (12). Uniqueness of the solution of (12) follows by applying the same estimate to the difference of two solutions.

Finally, the choice $\eta = C_s \mu^{-1}$ follows immediately from the scattering boundedness estimate in Theorem 3.1. \square

4. ANGULAR APPROXIMATION AND ERROR CONTROL

In this section we focus on the angular discretisation of elastic Coulomb scattering. For simplicity we neglect nonelastic interactions and retain only the energy-conserving elastic component of the gain. Accordingly we work with an elastic kernel $\sigma_{\text{el}}(\omega, \omega', E)$ and the associated gain

$$\mathcal{K}_{\text{el}}[\psi](\mathbf{x}, E, \omega) := \int_{\mathbb{S}^{d-1}} \sigma_{\text{el}}(\omega, \omega', E) \psi(\mathbf{x}, E, \omega') d\omega'.$$

The stopping power $S(E)$ is the same as in Section 2.

To reduce computational cost, we restrict the angular domain to a forward cone centred on the primary beam direction. Let $\omega_* \in \mathbb{S}^{d-1}$ be a reference direction and, for a half-angle $\theta_c > 0$, define

$$(18) \quad \mathcal{C}(\omega_*, \theta_c) := \left\{ \omega' \in \mathbb{S}^{d-1} : \arccos(\omega_* \cdot \omega') \leq \theta_c \right\},$$

illustrated in Figure 4. In forward-peaked regimes (high energies, weak multiple scattering) one may take θ_c small, whereas stronger scattering requires a larger cone.

We therefore introduce the cone-truncated gain operator

$$\mathcal{K}_{\text{el}}^c[\psi](\mathbf{x}, E, \omega) := \int_{\mathcal{C}(\omega_*, \theta_c)} \sigma_{\text{el}}(\omega, \omega', E) \psi(\mathbf{x}, E, \omega') d\omega'.$$

The difference $\mathcal{K}_{\text{el}}[\psi] - \mathcal{K}_{\text{el}}^c[\psi]$ is the cone-truncation remainder, and it will be treated as a distinct error contribution below.

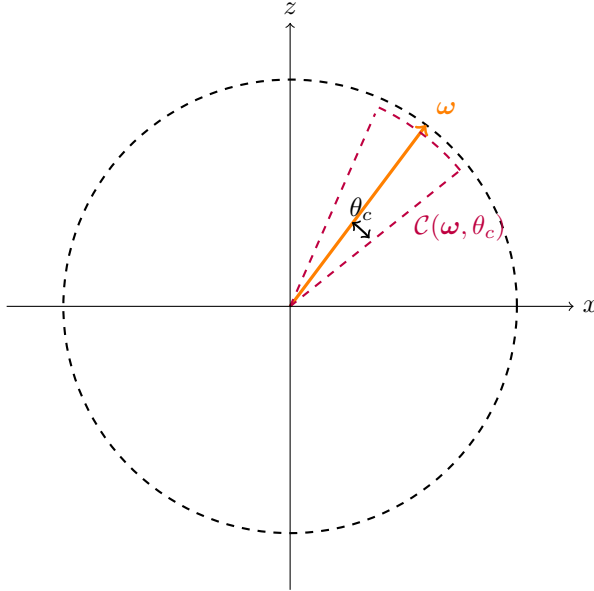


FIGURE 4. Angular computational domain restricted to a cone centred on ω_* .

4.1. Angular discretisation. Let $\{\omega_j\}_{j=1}^Q \subset \mathcal{C}(\omega_*, \theta_c)$ be quadrature nodes with weights $\{\mu_j\}_{j=1}^Q > 0$. For sufficiently regular f ,

$$(19) \quad \int_{\mathcal{C}(\omega_*, \theta_c)} f(\omega') d\omega' \approx \sum_{j=1}^Q \mu_j f(\omega_j).$$

Applying (19) to the cone-truncated elastic gain yields

$$(20) \quad \int_{\mathcal{C}(\omega_*, \theta_c)} \sigma_{\text{el}}(\omega, \omega', E) \psi(\mathbf{x}, E, \omega') d\omega' \approx \sum_{j=1}^Q \mu_j \sigma_{\text{el}}(\omega, \omega_j, E) \psi(\mathbf{x}, E, \omega_j).$$

Introducing the directional unknowns $\psi_i(\mathbf{x}, E) := \psi(\mathbf{x}, E, \boldsymbol{\omega}_i)$ for $i = 1, \dots, Q$, the corresponding discrete-ordinates system for the cone-truncated model reads

$$(21) \quad \boldsymbol{\omega}_i \cdot \nabla_{\mathbf{x}} \psi_i(\mathbf{x}, E) - \partial_E(S(E)\psi_i(\mathbf{x}, E)) + \sigma_T(E)\psi_i(\mathbf{x}, E) = \sum_{j=1}^Q \mu_j \sigma_{\text{el}}(\boldsymbol{\omega}_i, \boldsymbol{\omega}_j, E) \psi_j(\mathbf{x}, E), \quad i = 1, \dots, Q.$$

This is a coupled family of energy-dependent transport equations, one per direction, capturing forward-peaked angular exchange within $\mathcal{C}(\boldsymbol{\omega}_*, \theta_c)$. For each ordinate i , the inflow boundary condition is imposed on $\Gamma_-(\boldsymbol{\omega}_i)$ in the sense of Section 2, namely on the spatial inflow set $\{\boldsymbol{\omega}_i \cdot \mathbf{n}_{\mathbf{x}} < 0\}$ together with the top-energy boundary $E = E_{\max}$, with no condition on the corresponding outflow.

4.2. Remark (Continuum conservation). *Assume the elastic kernel satisfies the mass-conserving normalisation*

$$\int_{\mathbb{S}^{d-1}} \sigma_{\text{el}}(\boldsymbol{\omega}, \boldsymbol{\omega}', E) d\boldsymbol{\omega} = \Sigma_{\text{el}}(E) \quad \text{for a.e. } E \in I,$$

where $\Sigma_{\text{el}}(E)$ is independent of $\boldsymbol{\omega}'$. Then the elastic gain satisfies the identity

$$\int_{\mathbb{S}^{d-1}} \left(\int_{\mathbb{S}^{d-1}} \sigma_{\text{el}}(\boldsymbol{\omega}, \boldsymbol{\omega}', E) \psi(\mathbf{x}, E, \boldsymbol{\omega}') d\boldsymbol{\omega}' \right) d\boldsymbol{\omega} = \Sigma_{\text{el}}(E) \int_{\mathbb{S}^{d-1}} \psi(\mathbf{x}, E, \boldsymbol{\omega}) d\boldsymbol{\omega}.$$

Consequently, in the purely elastic setting where the loss term contains the elastic removal $\Sigma_{\text{el}}(E)\psi$ (for example $\sigma_T(E) = \Sigma_{\text{el}}(E)$ when no other interactions are present), the net elastic scattering contribution conserves particle number at each energy after integrating over \mathbb{S}^{d-1} .

If the angular domain is truncated to a cone $\mathcal{C}(\boldsymbol{\omega}_*, \theta_c)$, then the corresponding cone-truncated gain $\mathcal{K}_{\text{el}}^c$ fails to satisfy the full-sphere identity only through scattering events that transfer mass to $\mathbb{S}^{d-1} \setminus \mathcal{C}(\boldsymbol{\omega}_*, \theta_c)$. Quantitative bounds are given later via cone-truncation error estimates.

4.3. Proposition (Discrete conservation under exact angular quadrature). *Assume the elastic kernel is rotationally invariant at fixed energy, $\sigma_{\text{el}}(\boldsymbol{\omega}, \boldsymbol{\omega}', E) = \kappa_E(\boldsymbol{\omega} \cdot \boldsymbol{\omega}')$ with $\kappa_E : [-1, 1] \rightarrow \mathbb{R}_+$. Fix an integer $L \geq 0$ and assume that, for a.e. $E \in I$, κ_E admits a truncated Legendre expansion of degree at most L , that is,*

$$\kappa_E(\mu) = \sum_{\ell=0}^L a_{\ell}(E) P_{\ell}(\mu) \quad \text{for } \mu \in [-1, 1],$$

with coefficients $a_{\ell}(E) \geq 0$. Let $\{(\boldsymbol{\omega}_i, \varpi_i)\}_{i=1}^Q \subset \mathbb{S}^{d-1} \times (0, \infty)$ be a full-sphere quadrature rule that is exact for spherical harmonics (up to degree L), equivalently exact for all restrictions to \mathbb{S}^{d-1} of polynomials in $\boldsymbol{\omega}$ of total degree at most L . In particular, for each $j = 1, \dots, Q$ and a.e. $E \in I$, this implies exactness for the corresponding zonal functions $\boldsymbol{\omega} \mapsto P_{\ell}(\boldsymbol{\omega} \cdot \boldsymbol{\omega}_j)$, $\ell = 0, \dots, L$, and hence for $\boldsymbol{\omega} \mapsto \kappa_E(\boldsymbol{\omega} \cdot \boldsymbol{\omega}_j)$. Define

$$\Sigma_{\text{el}}(E) := \int_{\mathbb{S}^{d-1}} \sigma_{\text{el}}(\boldsymbol{\omega}, \boldsymbol{\omega}', E) d\boldsymbol{\omega},$$

which is independent of $\boldsymbol{\omega}'$ by rotational invariance. Then for any values $\{\psi_j(\mathbf{x}, E)\}_{j=1}^Q$ one has the discrete balance

$$\sum_{i=1}^Q \varpi_i \left(\sum_{j=1}^Q \mu_j \sigma_{\text{el}}(\boldsymbol{\omega}_i, \boldsymbol{\omega}_j, E) \psi_j(\mathbf{x}, E) - \Sigma_{\text{el}}(E) \psi_i(\mathbf{x}, E) \right) = 0,$$

where $\psi_i(\mathbf{x}, E) := \psi(\mathbf{x}, E, \boldsymbol{\omega}_i)$. Equivalently,

$$\sum_{i=1}^Q \varpi_i \sum_{j=1}^Q \mu_j \sigma_{\text{el}}(\boldsymbol{\omega}_i, \boldsymbol{\omega}_j, E) \psi_j(\mathbf{x}, E) = \Sigma_{\text{el}}(E) \sum_{i=1}^Q \varpi_i \psi_i(\mathbf{x}, E).$$

Proof. Using $\sigma_{\text{el}}(\boldsymbol{\omega}_i, \boldsymbol{\omega}_j, E) = \kappa_E(\boldsymbol{\omega}_i \cdot \boldsymbol{\omega}_j)$, we compute

$$\sum_{i=1}^Q \varpi_i \sum_{j=1}^Q \mu_j \sigma_{\text{el}}(\boldsymbol{\omega}_i, \boldsymbol{\omega}_j, E) \psi_j = \sum_{j=1}^Q \mu_j \psi_j \left(\sum_{i=1}^Q \varpi_i \kappa_E(\boldsymbol{\omega}_i \cdot \boldsymbol{\omega}_j) \right).$$

By quadrature exactness, for each fixed j we have

$$\sum_{i=1}^Q \varpi_i \kappa_E(\boldsymbol{\omega}_i \cdot \boldsymbol{\omega}_j) = \int_{\mathbb{S}^{d-1}} \kappa_E(\boldsymbol{\omega} \cdot \boldsymbol{\omega}_j) d\boldsymbol{\omega} = \int_{\mathbb{S}^{d-1}} \sigma_{\text{el}}(\boldsymbol{\omega}, \boldsymbol{\omega}_j, E) d\boldsymbol{\omega} = \Sigma_{\text{el}}(E),$$

and the right-hand side is independent of j . Substituting gives

$$\sum_{i=1}^Q \varpi_i \sum_{j=1}^Q \mu_j \sigma_{\text{el}}(\boldsymbol{\omega}_i, \boldsymbol{\omega}_j, E) \psi_j = \Sigma_{\text{el}}(E) \sum_{j=1}^Q \mu_j \psi_j,$$

which is equivalent to the stated balance. \square

4.4. Remark. *Exact conservation in Proposition 4.3 relies on a full-sphere quadrature rule that is exact for the relevant zonal functions. In the cone-restricted setting $\mathcal{C}(\boldsymbol{\omega}_*, \theta_c)$ used for computation, the same calculation applies to the cone-truncated gain, but conservation holds only up to a remainder representing scattering events that transfer mass to $\mathbb{S}^{d-1} \setminus \mathcal{C}(\boldsymbol{\omega}_*, \theta_c)$. Quantitative bounds are given later via cone-truncation estimates.*

Let $U := L^2(D \times I)$ and write $\mathbf{u} = (u_1, \dots, u_Q) \in U^Q$ for the directional components associated with nodes $\{\boldsymbol{\omega}_i\}_{i=1}^Q$. We work with the per-ordinate graph spaces

$$\mathcal{U}_i := \left\{ w \in L^2(D \times I) : \boldsymbol{\omega}_i \cdot \nabla_{\mathbf{x}} w \in L^2(D \times I), \partial_E(S(E)w) \in L^2(D \times I) \right\}, \quad i = 1, \dots, Q,$$

and the product space $\mathcal{U}^Q := \prod_{i=1}^Q \mathcal{U}_i$. We write $d\gamma$ for the surface measure on $\partial(D \times I)$.

The discrete elastic scattering form for the i -th direction is

$$(22) \quad s^Q(\mathbf{u}, v_i; \boldsymbol{\omega}_i) := \int_D \int_I v_i(\mathbf{x}, E) \sum_{j=1}^Q \mu_j \sigma_{\text{el}}(\boldsymbol{\omega}_i, \boldsymbol{\omega}_j, E) u_j(\mathbf{x}, E) dE d\mathbf{x}.$$

Consistently with Section 3, the directional bilinear form retains the transport and boundary terms,

$$(23) \quad a(u_i, v_i; \boldsymbol{\omega}_i) := \int_D \int_I \left[(\boldsymbol{\omega}_i \cdot \nabla_{\mathbf{x}} u_i) v_i - \partial_E(S(E)u_i) v_i + \sigma_T(E) u_i v_i \right] dE d\mathbf{x} + \frac{1}{2} \int_{\Gamma_+(\boldsymbol{\omega}_i)} (\boldsymbol{\omega}_i \cdot \mathbf{n}_{\mathbf{x}} - S(E)n_E) u_i v_i d\gamma,$$

and the inflow linear form for the i -th direction is

$$(24) \quad l(v_i; \boldsymbol{\omega}_i) := -\frac{1}{2} \int_{\Gamma_-(\boldsymbol{\omega}_i)} (\boldsymbol{\omega}_i \cdot \mathbf{n}_{\mathbf{x}} - S(E)n_E) g(\mathbf{x}, E, \boldsymbol{\omega}_i) v_i(\mathbf{x}, E) d\gamma.$$

Neglecting nonelastic interactions, the discrete weak problem in angle is: find $\mathbf{u} \in \mathcal{U}^Q$ such that, for each $i = 1, \dots, Q$,

$$(25) \quad a(u_i, v_i; \boldsymbol{\omega}_i) = s^Q(\mathbf{u}, v_i; \boldsymbol{\omega}_i) + l(v_i; \boldsymbol{\omega}_i) \quad \text{for all } v_i \in \mathcal{U}_i.$$

4.5. Source iteration. The coupled directional system (21) contains angular scattering terms that redistribute particles across directions. We utilise a discrete source-iteration scheme, which decouples the directional equations at each step and permits independent, parallel directional solves.

Given $\mathbf{u}^{(0)} = (u_1^{(0)}, \dots, u_Q^{(0)}) \in \mathcal{U}^Q$, define $\mathbf{u}^{(n)} = (u_1^{(n)}, \dots, u_Q^{(n)})$ by, for each $i = 1, \dots, Q$,

$$(26) \quad \boldsymbol{\omega}_i \cdot \nabla_{\mathbf{x}} u_i^{(n)}(\mathbf{x}, E) - \partial_E(S(E)u_i^{(n)}(\mathbf{x}, E)) + \sigma_T(E) u_i^{(n)}(\mathbf{x}, E) = \sum_{j=1}^Q \mu_j \sigma_{\text{el}}(\boldsymbol{\omega}_i, \boldsymbol{\omega}_j, E) u_j^{(n-1)}(\mathbf{x}, E),$$

with inflow data $u_i^{(n)} = g(\cdot, \cdot, \boldsymbol{\omega}_i)$ on $\Gamma_-(\boldsymbol{\omega}_i)$.

The corresponding discrete weak formulation reads: given $\mathbf{u}^{(n-1)} \in \mathcal{U}^Q$, find $\mathbf{u}^{(n)} \in \mathcal{U}^Q$ such that, for each $i = 1, \dots, Q$,

$$(27) \quad a(u_i^{(n)}, v_i; \boldsymbol{\omega}_i) = s^Q(\mathbf{u}^{(n-1)}, v_i; \boldsymbol{\omega}_i) + l(v_i; \boldsymbol{\omega}_i) \quad \text{for all } v_i \in \mathcal{U}_i.$$

4.6. Proposition (Convergence of discrete-ordinates source iteration). *Assume the hypotheses of Theorem 3.1 and neglect nonelastic interactions, so that scattering is given by the elastic kernel σ_{el} . Let $\{\omega_i, \varpi_i\}_{i=1}^Q$ be a (full-sphere or cone-restricted) quadrature rule and consider the discrete-ordinates weak iteration (27) on the product graph space $\mathcal{U}^Q = \prod_{i=1}^Q \mathcal{U}_i$.*

Assume that the discrete scattering form satisfies the boundedness estimate: there exists $\eta_Q \geq 0$ such that

$$(28) \quad \left| \sum_{i=1}^Q \varpi_i s^Q(\mathbf{w}, \mathbf{v}_i; \omega_i) \right| \leq \eta_Q \|\mathbf{w}\|_{\mathcal{U}^Q} \|\mathbf{v}\|_{\mathcal{U}^Q} \quad \text{for all } \mathbf{w}, \mathbf{v} \in \mathcal{U}^Q,$$

where $\|\mathbf{w}\|_{\mathcal{U}^Q}^2 := \sum_{i=1}^Q \varpi_i \|w_i\|_{\mathcal{U}_i}^2$ and $\|\cdot\|_{\mathcal{U}_i}$ is the coercivity norm induced by $a(\cdot, \cdot; \omega_i)$.

If $2\eta_Q < 1$, then the discrete source iteration (27) is a strict contraction on \mathcal{U}^Q in the norm $\|\cdot\|_{\mathcal{U}^Q}$. Consequently, for any initial guess $\mathbf{u}^{(0)} \in \mathcal{U}^Q$ the iterates $\mathbf{u}^{(n)}$ converge strongly in \mathcal{U}^Q to the unique solution $\mathbf{u} \in \mathcal{U}^Q$ of the discrete weak problem (25).

Proof. The argument is identical to the continuum proof of Proposition 3.3, with the integrated forms over \mathbb{S}^{d-1} replaced by the quadrature sums $\sum_{i=1}^Q \varpi_i(\cdot)$ and with the space \mathcal{U} replaced by the product graph space \mathcal{U}^Q . In particular, taking differences between successive iterates eliminates the fixed inflow datum, so the error has homogeneous inflow trace on each $\Gamma_-(\omega_i)$. Testing the discrete error equation with the discrete error, applying coercivity of the transport part (the discrete analogue of Theorem 3.1 with ω fixed to ω_i), and then using (28) yields the contraction factor $2\eta_Q$. \square

5. ERROR CONTROL FOR THE ANGULAR APPROXIMATION

This section quantifies the error introduced by restricting and discretising angle and by terminating the source iteration. Throughout we work with the elastic model of Section 4, that is, (4) with the gain replaced by the elastic operator.

5.1. Setting and error decomposition. Let \mathcal{A} denote either \mathbb{S}^{d-1} or the cone $\mathcal{C}(\omega_*, \theta_c)$ from (18). Define the \mathcal{A} -restricted elastic gain

$$\mathcal{K}_{\text{el}}^{\mathcal{A}}[\psi](\mathbf{x}, E, \omega) := \int_{\mathcal{A}} \sigma_{\text{el}}(\omega, \omega', E) \psi(\mathbf{x}, E, \omega') d\omega'.$$

Let $\psi^{\mathcal{A}}$ denote the corresponding continuum solution of (4) with \mathcal{K}_{el} replaced by $\mathcal{K}_{\text{el}}^{\mathcal{A}}$. In particular, $\psi^{\mathbb{S}^{d-1}} = \psi$.

Fix an angular domain $\mathcal{A} \subseteq \mathbb{S}^{d-1}$ (either \mathbb{S}^{d-1} or a cone) and an angular rule $\{(\omega_j, w_j)\}_{j=1}^Q \subset \mathcal{A} \times (0, \infty)$. Let $\psi^{\mathcal{A}}$ denote the continuum solution of the elastic transport problem in which the gain integral is restricted to \mathcal{A} . Let $\{\psi_i^Q\}_{i=1}^Q$ denote the exact solution of the coupled Q -direction discrete-ordinates system (21) posed on \mathcal{A} with the same angular rule, and let $\{\psi_i^{Q,n}\}_{i=1}^Q$ be the n th source-iteration iterate.

Then, for each node ω_i ,

$$(29) \quad \psi(\cdot, \cdot, \omega_i) - \psi_i^{Q,n} = (\psi(\cdot, \cdot, \omega_i) - \psi^{\mathcal{A}}(\cdot, \cdot, \omega_i)) + (\psi^{\mathcal{A}}(\cdot, \cdot, \omega_i) - \psi_i^Q) + (\psi_i^Q - \psi_i^{Q,n}).$$

The first term is a model-truncation contribution, it vanishes when $\mathcal{A} = \mathbb{S}^{d-1}$ (since then $\psi^{\mathcal{A}} = \psi$), and when \mathcal{A} is a cone it measures the effect of omitting scattering into directions outside \mathcal{A} . The second term is the discrete-ordinates (quadrature/collocation) contribution for the \mathcal{A} -restricted model, it compares the continuum solution $\psi^{\mathcal{A}}$ sampled at ω_i with the exact coupled DOM solution on the same ordinates. The third term is the source-iteration contribution for solving the coupled DOM system.

To transfer gain consistency bounds into solution bounds we use the directional coercivity norm induced by the transport form. For each direction ω_i define

$$\|w\|_{\mathcal{U}_i}^2 := \|\sigma_T^{1/2} w\|_{L^2(D \times I)}^2 + \|(-S')^{1/2} w\|_{L^2(D \times I)}^2 + \int_{\Gamma_+(\omega_i)} (\omega_i \cdot \mathbf{n}_{\mathbf{x}} - S(E) n_E) w^2 d\gamma,$$

and the weighted product norm

$$\|\mathbf{w}\|_{\mathcal{U}^Q}^2 := \sum_{i=1}^Q \varpi_i \|w_i\|_{\mathcal{U}_i}^2.$$

5.2. Lemma (Directional stability). *Fix ω_i and consider two right-hand sides $F, \tilde{F} \in \mathcal{U}'_i$ and two solutions $u, \tilde{u} \in \mathcal{U}_i$ with the same inflow data such that*

$$a(u, v; \omega_i) = F(v), \quad a(\tilde{u}, v; \omega_i) = \tilde{F}(v) \quad \text{for all } v \in \mathcal{U}_i.$$

Then

$$\|u - \tilde{u}\|_{\mathcal{U}_i} \leq 2\|F - \tilde{F}\|_{\mathcal{U}'_i}.$$

Proof. Subtract the two identities and test with $v = u - \tilde{u}$. The error has homogeneous inflow trace, so Theorem 3.1 gives $\frac{1}{2}\|u - \tilde{u}\|_{\mathcal{U}_i}^2 \leq |(F - \tilde{F})(u - \tilde{u})| \leq \|F - \tilde{F}\|_{\mathcal{U}'_i}\|u - \tilde{u}\|_{\mathcal{U}_i}$. \square

5.3. Quadrature consistency on \mathcal{A} . For an integrand $f : \mathcal{A} \rightarrow \mathbb{R}$ set

$$I_{\mathcal{A}}(f) := \int_{\mathcal{A}} f(\omega) d\omega, \quad Q_{\mathcal{A}}(f) := \sum_{j=1}^Q \mu_j f(\omega_j).$$

Define the angular fill distance

$$h_{\omega} := \sup_{\omega \in \mathcal{A}} \min_{1 \leq j \leq Q} \arccos(\omega \cdot \omega_j).$$

If the rule is exact for spherical polynomials on \mathcal{A} up to total degree m and $f \in W^{m+1,1}(\mathcal{A})$, then there exists $C = C(m, d)$ such that

$$(30) \quad |I_{\mathcal{A}}(f) - Q_{\mathcal{A}}(f)| \leq Ch_{\omega}^{m+1} \sum_{|\alpha|=m+1} \|D_{\tan}^{\alpha} f\|_{L^1(\mathcal{A})}.$$

Applied pointwise in (\mathbf{x}, E) to the elastic gain integrand $f(\omega') = \sigma_{\text{el}}(\omega_i, \omega', E)\psi^{\mathcal{A}}(\mathbf{x}, E, \omega')$, (30) bounds the gain consistency defect

$$(\mathcal{K}_{\text{el}}^{\mathcal{A}}[\psi^{\mathcal{A}}])(\mathbf{x}, E, \omega_i) - \sum_{j=1}^Q \mu_j \sigma_{\text{el}}(\omega_i, \omega_j, E) \psi^{\mathcal{A}}(\mathbf{x}, E, \omega_j).$$

Using Lemma 5.2 yields the corresponding bound on $\psi_i^{\mathcal{A}} - \psi_i^Q$.

5.4. Proposition (Quadrature-induced angular discretisation error). *Assume the hypotheses of Theorem 3.1. Assume moreover that the angular rule on \mathcal{A} is exact for spherical polynomials up to degree m and that for each i the gain integrand $\omega' \mapsto \sigma_{\text{el}}(\omega_i, \omega', E)\psi^{\mathcal{A}}(\mathbf{x}, E, \omega')$ belongs to $W^{m+1,1}(\mathcal{A})$ for a.e. $(\mathbf{x}, E) \in D \times I$, with tangential derivatives integrable in (\mathbf{x}, E) . Then there exists $C_{\text{ang}} = C(m, d) > 0$ such that for each $i = 1, \dots, Q$,*

$$\|\psi_i^{\mathcal{A}} - \psi_i^Q\|_{\mathcal{U}_i} \leq C_{\text{ang}} h_{\omega}^{m+1} \Xi_{m+1}^{(i)}(\psi^{\mathcal{A}}, \sigma_{\text{el}}),$$

where

$$\Xi_{m+1}^{(i)}(\psi^{\mathcal{A}}, \sigma_{\text{el}}) := \sum_{|\alpha|=m+1} \|D_{\tan}^{\alpha}(\sigma_{\text{el}}(\omega_i, \cdot, E)\psi^{\mathcal{A}}(\mathbf{x}, E, \cdot))\|_{L^1(D \times I; L^1(\mathcal{A}))}.$$

5.5. Cone truncation. If $\mathcal{A} = \mathbb{S}^{d-1}$ this contribution vanishes. Otherwise $\mathcal{A} = \mathcal{C}(\omega_*, \theta_c)$ and the truncated gain omits scattering from $\mathbb{S}^{d-1} \setminus \mathcal{C}(\omega_*, \theta_c)$. For any $f : \mathbb{S}^{d-1} \rightarrow \mathbb{R}$,

$$\int_{\mathbb{S}^{d-1}} f(\omega') d\omega' - \int_{\mathcal{C}(\omega_*, \theta_c)} f(\omega') d\omega' = \int_{\mathbb{S}^{d-1} \setminus \mathcal{C}(\omega_*, \theta_c)} f(\omega') d\omega'.$$

A crude estimate is

$$(31) \quad \left| \int_{\mathbb{S}^{d-1} \setminus \mathcal{C}(\omega_*, \theta_c)} f(\omega') d\omega' \right| \leq \sup_{\omega' \in \mathbb{S}^{d-1} \setminus \mathcal{C}(\omega_*, \theta_c)} |f(\omega')| |\mathbb{S}^{d-1} \setminus \mathcal{C}(\omega_*, \theta_c)|.$$

Moreover, for forward-peaked kernels a more informative measure is the cone tail

$$e_{\text{cone}}(E) := \sup_{\omega \in \mathcal{C}(\omega_*, \theta_c)} \int_{\mathbb{S}^{d-1} \setminus \mathcal{C}(\omega_*, \theta_c)} \sigma_{\text{el}}(\omega, \omega', E) d\omega'.$$

This quantity measures the missing elastic gain at energy E . It enters (29) through the truncation term $\psi(\cdot, \cdot, \omega_i) - \psi^{\mathcal{A}}(\cdot, \cdot, \omega_i)$.

5.6. Source-iteration error and stopping. By Proposition 4.6, the discrete source iteration is a contraction in \mathcal{U}^Q provided the discrete scattering operator has bound η_Q in $\|\cdot\|_{\mathcal{U}^Q}$ satisfying $2\eta_Q < 1$. With $\rho := 2\eta_Q \in (0, 1)$ and $\mathbf{u}^{(\infty)}$ denoting the exact solution of (25),

$$(32) \quad \|\mathbf{u}^{(n)} - \mathbf{u}^{(\infty)}\|_{\mathcal{U}^Q} \leq \rho^n \|\mathbf{u}^{(0)} - \mathbf{u}^{(\infty)}\|_{\mathcal{U}^Q},$$

and the contraction property yields the a posteriori estimate

$$(33) \quad \|\mathbf{u}^{(n)} - \mathbf{u}^{(\infty)}\|_{\mathcal{U}^Q} \leq \frac{\rho}{1 - \rho} \|\mathbf{u}^{(n)} - \mathbf{u}^{(n-1)}\|_{\mathcal{U}^Q}.$$

Hence, for a prescribed tolerance $\varepsilon > 0$, it suffices to stop when

$$\|\mathbf{u}^{(n)} - \mathbf{u}^{(n-1)}\|_{\mathcal{U}^Q} \leq \frac{1 - \rho}{\rho} \varepsilon.$$

5.7. Theorem (Angular discretisation, truncation and iteration error). *Assume the hypotheses of Theorem 3.1. Fix $\mathcal{A} \in \{\mathbb{S}^{d-1}, \mathcal{C}(\omega_*, \theta_c)\}$ and a quadrature rule $\{(\omega_j, \mu_j)\}_{j=1}^Q \subset \mathcal{A} \times (0, \infty)$ with fill distance h_ω . Let ψ be the full-sphere continuum solution, let $\psi^{\mathcal{A}}$ be the \mathcal{A} -restricted continuum solution and let $\psi_i^{Q,n}$ be the n th source-iteration iterate for the coupled Q -direction discrete-ordinates system posed on \mathcal{A} .*

Assume that the quadrature hypotheses of Proposition 5.4 hold and that the discrete source iteration is contractive with factor $\rho \in (0, 1)$ so that (33) holds. Then for each node ω_i there exist constants $C_{\text{ang}} > 0$ and $C_{\text{stab}} > 0$ such that

$$(34) \quad \|\psi(\cdot, \cdot, \omega_i) - \psi_i^{Q,n}\|_{\mathcal{U}_i} \leq \|(\psi - \psi^{\mathcal{A}})(\cdot, \cdot, \omega_i)\|_{\mathcal{U}_i} + C_{\text{ang}} h_\omega^{m+1} \Xi_{m+1}^{(i)}(\psi^{\mathcal{A}}, \sigma_{\text{el}}) + C_{\text{stab}} \frac{\rho}{1 - \rho} \|\mathbf{u}^{(n)} - \mathbf{u}^{(n-1)}\|_{\mathcal{U}^Q}.$$

If $\mathcal{A} = \mathbb{S}^{d-1}$ the first term vanishes. If $\mathcal{A} = \mathcal{C}(\omega_*, \theta_c)$, the first term is the cone-truncation contribution and can be estimated in terms of the cone tail $e_{\text{cone}}(E)$ from Section 5.5 under additional control of ψ outside the cone.

Proof. Apply the decomposition (29). Bound $\psi_i^{\mathcal{A}} - \psi_i^Q$ by Proposition 5.4. Bound $\psi_i^Q - \psi_i^{Q,n}$ by (33) and the embedding $\|\psi_i^Q - \psi_i^{Q,n}\|_{\mathcal{U}_i} \leq C_{\text{stab}} \|\mathbf{u}^{(\infty)} - \mathbf{u}^{(n)}\|_{\mathcal{U}^Q}$. \square

5.8. Corollary (Separable tolerance allocation). *In the setting of Theorem 5.7, a sufficient condition for $\|\psi(\cdot, \cdot, \omega_i) - \psi_i^{Q,n}\|_{\mathcal{U}_i} \leq \varepsilon$ is*

$$\|(\psi - \psi_i^{\mathcal{A}})(\cdot, \cdot, \omega_i)\|_{\mathcal{U}_i} \leq \frac{\varepsilon}{3}, \quad C_{\text{ang}} h_\omega^{m+1} \Xi_{m+1}^{(i)}(\psi^{\mathcal{A}}, \sigma_{\text{el}}) \leq \frac{\varepsilon}{3}, \quad \frac{\rho}{1 - \rho} \|\mathbf{u}^{(n)} - \mathbf{u}^{(n-1)}\|_{\mathcal{U}^Q} \leq \frac{\varepsilon}{3C_{\text{stab}}}.$$

5.9. Example (Henyey–Greenstein on \mathbb{S}^1). Let

$$p_\gamma(\theta) = \frac{1}{2\pi} \frac{1 - \gamma^2}{1 + \gamma^2 - 2\gamma \cos(\theta)},$$

with θ the angle from ω_* . For $\gamma = 0.95$ and $\theta_c = \pi/2$, the supremum of p_γ on the excluded set $|\theta| \in [\theta_c, \pi]$ occurs at $|\theta| = \theta_c$, giving

$$\sup_{\theta \in [\theta_c, \pi]} p_\gamma(\theta) = \frac{1}{2\pi} \frac{1 - \gamma^2}{1 + \gamma^2 - 2\gamma \cos(\theta)_c} \approx 8.16 \times 10^{-3}.$$

Multiplying by the excluded arc length $2(\pi - \theta_c) = \pi$ yields the bound $|I - I_c| \lesssim 2.56 \times 10^{-2}$. For $\theta_c = 3\pi/4$, the same calculation gives $|I - I_c| \lesssim 7.5 \times 10^{-3}$.

6. NUMERICAL EXPERIMENTS: PROTON TRANSPORT

We now present numerical experiments to verify correctness of the discretisation, assess convergence of the source iteration scheme and investigate behaviour across representative forward-peaked scattering regimes. All simulations are conducted using a uniform Cartesian mesh and a piecewise constant angular discretisation unless stated otherwise.

6.1. Implementation of the numerical algorithm. We solve the angularly discrete transport system by source iteration, using the same discrete-ordinates quadrature framework as in Section 4. In particular, we work with quadrature nodes $\{\boldsymbol{\omega}_j\}_{j=1}^Q$ and weights $\{\mu_j\}_{j=1}^Q$ on the chosen angular domain (full sphere or cone). The angularly discrete unknowns are the directional values

$$\Psi_j(\mathbf{x}, E) := \psi(\mathbf{x}, E, \boldsymbol{\omega}_j), \quad j = 1, \dots, Q.$$

In these experiments we restrict to elastic Coulomb scattering and therefore use the elastic kernel σ_{el} from Section 4. The discrete elastic gain at node $\boldsymbol{\omega}_i$ is approximated by the midpoint quadrature rule,

$$(35) \quad \int_{\mathcal{A}} \sigma_{\text{el}}(\boldsymbol{\omega}_i, \boldsymbol{\omega}', E) \psi(\mathbf{x}, E, \boldsymbol{\omega}') d\boldsymbol{\omega}' \approx \sum_{j=1}^Q \mu_j \bar{\sigma}_{\text{el}}(\boldsymbol{\omega}_i, \boldsymbol{\omega}_j, E) \Psi_j(\mathbf{x}, E),$$

where $\bar{\sigma}_{\text{el}}(\boldsymbol{\omega}_i, \boldsymbol{\omega}_j, E)$ is a quadrature-consistent approximation of the kernel evaluated at the node $\boldsymbol{\omega}_j$ (in the simplest case, $\bar{\sigma}_{\text{el}}(\boldsymbol{\omega}_i, \boldsymbol{\omega}_j, E) = \sigma_{\text{el}}(\boldsymbol{\omega}_i, \boldsymbol{\omega}_j, E)$).

To ensure discrete conservation of total fluence (gain–loss balance), we enforce a discrete analogue of the identity in Proposition 4.3. Writing

$$\Sigma_{\text{el}}(E) := \int_{\mathbb{S}^{d-1}} \sigma_{\text{el}}(\boldsymbol{\omega}, \boldsymbol{\omega}', E) d\boldsymbol{\omega},$$

(which is independent of $\boldsymbol{\omega}'$ under rotational invariance), we impose the weighted row-sum condition

$$(36) \quad \sum_{i=1}^Q \varpi_i \bar{\sigma}_{\text{el}}(\boldsymbol{\omega}_i, \boldsymbol{\omega}_j, E) = \Sigma_{\text{el}}(E), \quad j = 1, \dots, Q.$$

Equivalently, for any angular vector $\{\Psi_j(\mathbf{x}, E)\}_{j=1}^Q$ one has

$$\sum_{i=1}^Q \varpi_i \sum_{j=1}^Q \mu_j \bar{\sigma}_{\text{el}}(\boldsymbol{\omega}_i, \boldsymbol{\omega}_j, E) \Psi_j(\mathbf{x}, E) = \Sigma_{\text{el}}(E) \sum_{j=1}^Q \mu_j \Psi_j(\mathbf{x}, E),$$

so the discrete elastic gain balances the corresponding loss in the weighted angular sum.

6.2. Remark (Relation to a finite-volume interpretation in angle). Although we implement scattering via quadrature nodes and weights, the formula (35) can be read as a finite-volume exchange between angular control volumes: the weights μ_j play the role of angular “cell measures”, while $\bar{\sigma}_{\text{el}}(\boldsymbol{\omega}_i, \boldsymbol{\omega}_j, E)$ acts as an energy-dependent transfer rate from direction $\boldsymbol{\omega}_j$ to $\boldsymbol{\omega}_i$. Condition (36) then corresponds to conservation of total fluence in the angular finite-volume balance.

When the angular domain is restricted to a forward cone, some fluence is necessarily lost at the boundary of the cone. In regimes where the scattering kernel is strongly forward-peaked (as is typical in proton and ion transport), this loss is negligible in practice.

The angularly discrete system seeks functions $\Psi_i : D \times I \rightarrow \mathbb{R}$ for $i = 1, \dots, Q$ satisfying

$$(37) \quad \boldsymbol{\omega}_i \cdot \nabla_{\mathbf{x}} \Psi_i(\mathbf{x}, E) - \partial_E(S(E) \Psi_i(\mathbf{x}, E)) + \sigma_T(E) \Psi_i(\mathbf{x}, E) = \sum_{j=1}^Q \mu_j \bar{\sigma}_{\text{el}}(\boldsymbol{\omega}_i, \boldsymbol{\omega}_j, E) \Psi_j(\mathbf{x}, E),$$

which is the discrete-ordinates model (21) with the elastic scattering sum realised via the quadrature-consistent coefficients $\bar{\sigma}_{\text{el}}$. We solve (37) by the source iteration method introduced in Section 4.5. The algorithmic structure is summarised in Algorithm 1.

6.3. Dose functional and discrete dose notation. The transport solver produces an approximation of the phase-space density $\psi(\mathbf{x}, E, \boldsymbol{\omega})$. In the numerical experiments we primarily report dose-like outputs obtained by integrating ψ against an energy-deposition weight. Concretely, for a given stopping power $S(E)$ we define the (unnormalised) dose functional

$$(38) \quad \mathcal{D}(\mathbf{x}) := \int_I \int_{\mathcal{A}} S(E) \psi(\mathbf{x}, E, \boldsymbol{\omega}) d\boldsymbol{\omega} dE,$$

Algorithm 1 Source iteration with method-of-characteristics (MoC) directional sweeps

Require: Quadrature nodes $\{\boldsymbol{\omega}_i\}_{i=1}^Q$ and weights $\{\varpi_i\}_{i=1}^Q$, Stopping power $S(E)$, removal $\sigma_T(E)$, elastic coupling $\bar{\sigma}_{\text{el}}(\boldsymbol{\omega}_i, \boldsymbol{\omega}_j, E)$, Inflow data $g(\mathbf{x}, E, \boldsymbol{\omega}_i)$ on $\Gamma_-(\boldsymbol{\omega}_i)$ for $i = 1, \dots, Q$, Tolerance $\text{TOL} > 0$, maximum iterations $N_{\text{max}} \in \mathbb{N}$

Ensure: An iterate $\mathbf{u}^{(n)} = (u_1^{(n)}, \dots, u_Q^{(n)})$ with $\|\mathbf{u}^{(n)} - \mathbf{u}^{(n-1)}\|_{\mathcal{U}^Q} \leq \text{TOL}$, or $n = N_{\text{max}}$

```

1: Initialisation (ballistic MoC sweep):
2: for  $i = 1$  to  $Q$  do
3:   Set  $G_i^{(0)}(\mathbf{x}, E) \leftarrow 0$ 
4:   Compute  $u_i^{(0)}$  by a MoC sweep in direction  $\boldsymbol{\omega}_i$ : integrate along characteristics of the drift  $(\boldsymbol{\omega}_i, -S(E))$  with inflow trace  $g(\cdot, \cdot, \boldsymbol{\omega}_i)$  and source  $G_i^{(0)}$ 
5: end for

6: for  $n = 1$  to  $N_{\text{max}}$  do
7:   Elastic gain assembly:
8:   for  $i = 1$  to  $Q$  do
9:      $G_i^{(n)}(\mathbf{x}, E) \leftarrow \sum_{j=1}^Q \mu_j \bar{\sigma}_{\text{el}}(\boldsymbol{\omega}_i, \boldsymbol{\omega}_j, E) u_j^{(n-1)}(\mathbf{x}, E)$ 
10:    end for
11:   Directional MoC sweeps:
12:   for  $i = 1$  to  $Q$  do
13:     Compute  $u_i^{(n)}$  by a MoC sweep in direction  $\boldsymbol{\omega}_i$ : evaluate  $u_i^{(n)}(\mathbf{x}, E)$  via the characteristic map and the line integral of  $G_i^{(n)}$  along characteristics of  $(\boldsymbol{\omega}_i, -S(E))$ , with inflow trace  $g(\cdot, \cdot, \boldsymbol{\omega}_i)$ 
14:   end for
15:    $\text{ERR} \leftarrow \|\mathbf{u}^{(n)} - \mathbf{u}^{(n-1)}\|_{\mathcal{U}^Q}$ 
16:   if  $\text{ERR} \leq \text{TOL}$  then
17:     break
18:   end if
19: end for

```

where $\mathcal{A} = \mathbb{S}^{d-1}$ in the full angular model and $\mathcal{A} = \mathcal{C}(\boldsymbol{\omega}_*, \theta_c)$ when a cone is used. (Any constant factors converting energy deposition to physical dose in Gy are absorbed into the overall normalisation in these tests.)

For the angularly discrete model with quadrature nodes $\{(\boldsymbol{\omega}_i, \varpi_i)\}_{i=1}^Q \subset \mathcal{A} \times (0, \infty)$, let $\Psi_i(\mathbf{x}, E)$ denote the computed directional solution at $\boldsymbol{\omega}_i$. The corresponding discrete dose is defined by replacing the angular integral in (38) by quadrature and evaluating the remaining energy integral numerically on the chosen energy grid:

$$(39) \quad \mathcal{D}^Q(\mathbf{x}) := \sum_{k=1}^{N_E} w_k \sum_{i=1}^Q \varpi_i S(E_k) \Psi_i(\mathbf{x}, E_k),$$

where $\{E_k, w_k\}_{k=1}^{N_E}$ are the energy nodes and weights used in the implementation. When a reference solution is available analytically, we compute the corresponding reference dose \mathcal{D} from (38) using the same energy quadrature to isolate the spatial discretisation error.

6.4. Experiment 1: Benchmarking against an exact transport solution. We first consider a degenerate limit in which scattering is absent in practice because the angular redistribution collapses to the identity. We model this by the distributional kernel

$$(40) \quad \sigma_{\text{el}}(\boldsymbol{\omega}, \boldsymbol{\omega}', E) = \Sigma_{\text{el}}(E) \delta(\boldsymbol{\omega} - \boldsymbol{\omega}'),$$

so that $\mathcal{K}_{\text{el}}[\psi](\mathbf{x}, E, \boldsymbol{\omega}) = \Sigma_{\text{el}}(E) \psi(\mathbf{x}, E, \boldsymbol{\omega})$. Choosing the removal to match, $\sigma_T(E) = \Sigma_{\text{el}}(E)$, the gain term cancels the loss term and (4) reduces to the pure transport–slowing-down equation

$$\boldsymbol{\omega} \cdot \nabla_{\mathbf{x}} \psi(\mathbf{x}, E, \boldsymbol{\omega}) - \partial_E(S(E) \psi(\mathbf{x}, E, \boldsymbol{\omega})) = 0,$$

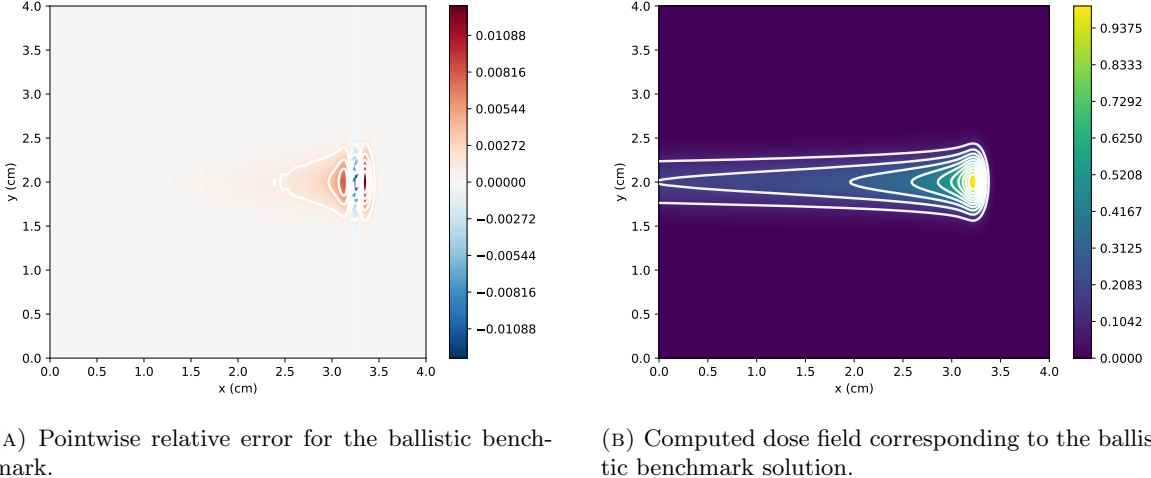
posed with the inflow condition $\psi = g$ on Γ_- . This case admits an explicit characteristic solution and therefore provides a stringent code-level benchmark for the method-of-characteristics sweep, including correct localisation along ω and correct propagation in energy.

In the Bragg–Kleeman setting $S(E) = \frac{1}{\alpha p} E^{1-p}$, an exact solution is

$$(41) \quad \psi(\mathbf{x}, E, \omega) = \left(E^p + \frac{\omega \cdot (\mathbf{x} - \mathbf{x}_0)}{\alpha} \right)^{\frac{1-p}{p}} E^{p-1} g \left(\left(E^p + \frac{\omega \cdot (\mathbf{x} - \mathbf{x}_0)}{\alpha} \right)^{\frac{1}{p}}, \mathbf{x}_0, \omega \right),$$

where $\mathbf{x}_0 = \mathbf{x}_0(\mathbf{x}, E, \omega) \in \partial D$ denotes the point where the characteristic through (\mathbf{x}, E) in direction ω meets the spatial inflow boundary (equivalently, the preimage under the characteristic map).

We compare the numerical approximation produced by the MoC sweep against the exact benchmark (41) through the induced dose field (38). Figure 5a displays the pointwise relative dose error $(\mathcal{D}^Q - \mathcal{D}) / \|\mathcal{D}\|_{L^\infty}$, and Figure 5b shows the corresponding computed dose field \mathcal{D}^Q for this ballistic transport case.



(a) Pointwise relative error for the ballistic benchmark.

(b) Computed dose field corresponding to the ballistic benchmark solution.

FIGURE 5. Ballistic (degenerate scattering) benchmark. Left: pointwise relative error of the numerical transport solution against the exact characteristic solution (41). Right: computed dose field for the same test case.

To quantify convergence under mesh refinement, we report the maximum pointwise dose error normalised by the peak reference dose,

$$\frac{\|\mathcal{D}^Q - \mathcal{D}\|_{L^\infty(D)}}{\|\mathcal{D}\|_{L^\infty(D)}} = \frac{\max_{\mathbf{x} \in D} |\mathcal{D}^Q(\mathbf{x}) - \mathcal{D}(\mathbf{x})|}{\max_{\mathbf{x} \in D} \mathcal{D}(\mathbf{x})}.$$

and plot it against the number of spatial cells N_x on a log–log scale. Figure 6 also shows an empirical power-law fit obtained by linear regression in logarithmic coordinates.

6.5. Experiment 2: Convergence of source iteration. We next examine convergence of the source-iteration scheme for the angularly discrete transport system on a fixed discretisation. We use the finest spatial and energy grids from Experiment 6.4 and the same angular rule as in the subsequent scattering runs. Fix an angular rule with Q directions. Let $\psi^{(n)} = (\psi_1^{(n)}, \dots, \psi_Q^{(n)}) \in U^Q$ denote the n th iterate produced by source iteration, where each component $\psi_i^{(n)}(\mathbf{x}, E) \approx \psi(\mathbf{x}, E, \omega_i)$ is computed by a single method-of-characteristics sweep in direction ω_i with a right-hand side assembled from the previous iterate.

To quantify convergence, we monitor the maximum successive-iterate difference over all directions and phase-space gridpoints,

$$(42) \quad \Delta_\infty^{(n)} := \max_{1 \leq i \leq Q} \|\psi_i^{(n)} - \psi_i^{(n-1)}\|_{L^\infty(D \times I)}.$$

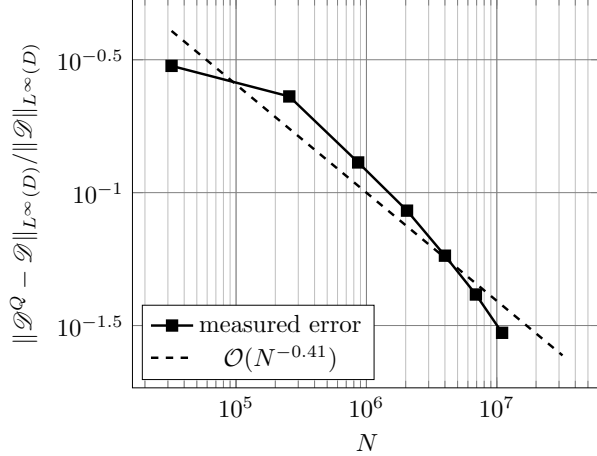


FIGURE 6. Convergence of the ballistic benchmark under spatial mesh refinement, measured by the maximum pointwise dose error normalised by the peak reference dose, $\|\mathcal{D}^Q - \mathcal{D}\|_{L^\infty(D)}/\|\mathcal{D}\|_{L^\infty(D)}$, plotted against $N = N_x N_y N_E$ on a log–log scale. The dashed line shows the empirical power-law fit.

This diagnostic is inexpensive to compute, is directly available from the stored iterates and provides a practical stopping proxy. In particular, when the discrete source iteration is contractive in the product graph norm, the a posteriori bound (33) implies that small successive differences $\|\psi^{(n)} - \psi^{(n-1)}\|_{\mathcal{U}^Q}$ control the distance to the converged discrete-ordinates solution. While $\Delta_\infty^{(n)}$ is not the same norm, in practice it tracks the same geometric decay and is therefore used here as a convenient stopping indicator.

Figure 7 plots $\Delta_\infty^{(n)}$ against the iteration count n on a logarithmic scale. For comparison we also plot a geometric reference curve of the form Cr^{n-1} with $C = \Delta_\infty^{(1)}$ and a representative contraction factor $r \in (0, 1)$. When the source iteration is contractive, one expects $\Delta_\infty^{(n)}$ to decay approximately geometrically until the iteration reaches the level of discretisation and floating-point errors.

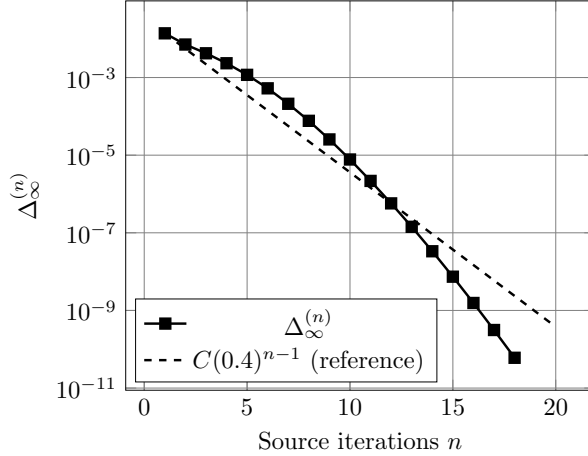


FIGURE 7. Convergence history of source iteration on the finest discretisation, measured by the successive-iterate difference $\Delta_\infty^{(n)} = \max_{1 \leq i \leq Q} \|\psi_i^{Q,n} - \psi_i^{Q,n-1}\|_{L^\infty(D \times I)}$. The dashed curve is a geometric reference line Cr^{n-1} with $C = \Delta_\infty^{(1)}$ and a representative $r \in (0, 1)$.

6.6. Experiment 3: Simulations with a Henyey–Greenstein cross section. To model anisotropic (forward-peaked) angular scattering we use the Henyey–Greenstein phase function on \mathbb{S}^1 ,

$$(43) \quad p_\gamma(\theta) = \frac{1}{2\pi} \frac{1 - \gamma^2}{1 + \gamma^2 - 2\gamma \cos(\theta)}, \quad \theta \in [-\pi, \pi),$$

which satisfies the normalisation $\int_{-\pi}^{\pi} p_\gamma(\theta) d\theta = 1$. For $\gamma \in (0, 1)$ the distribution is strongly forward-peaked, whereas $\gamma < 0$ corresponds to backscattering.

In these experiments we work in $d = 2$, so directions are parametrised by an angle θ via $\omega(\theta) = (\cos(\theta), \sin(\theta))$. We take an energy-independent, rotationally invariant elastic kernel of the form

$$\sigma_{\text{el}}(\omega(\theta), \omega(\theta')) = \Sigma_{\text{el}} p_\gamma(\theta - \theta'),$$

so that the corresponding gain is the circular convolution

$$\mathcal{K}_{\text{el}}[\psi](\mathbf{x}, E, \theta) = \Sigma_{\text{el}} \int_{-\pi}^{\pi} p_\gamma(\theta - \theta') \psi(\mathbf{x}, E, \theta') d\theta'.$$

This kernel is isotropic about the current direction in the sense that it depends only on the relative turning angle $\theta - \theta'$.

Figure 8 shows p_γ for $\gamma = 0.9$ together with its piecewise-constant approximation on the angular bins used in the computation. Concretely, if $\{B_j\}_{j=1}^Q$ is a partition of $[-\pi, \pi)$ with bin measures $\mu_j := |B_j|$ and midpoints $\theta_j \in B_j$, then the bar height in bin B_j is the bin average $\bar{p}_j := \mu_j^{-1} \int_{B_j} p_\gamma(\theta) d\theta$, so that $p_\gamma \approx \sum_{j=1}^Q \bar{p}_j \mathbf{1}_{B_j}$ and $\sum_{j=1}^Q \mu_j \bar{p}_j = 1$.

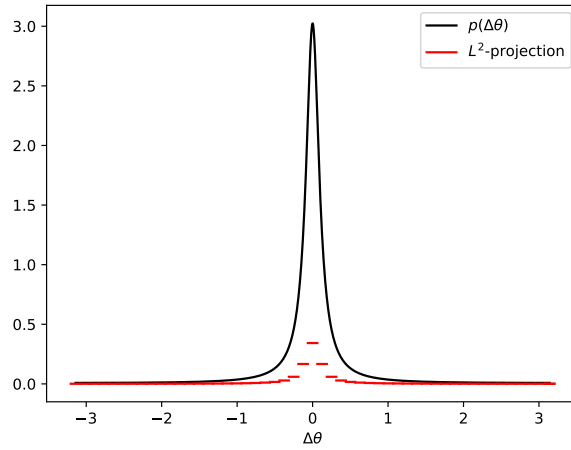


FIGURE 8. Henyey–Greenstein phase function (43) on \mathbb{S}^1 with anisotropy parameter $\gamma = 0.9$. The red bars show the bin averages \bar{p}_j on the piecewise-constant angular partition used to assemble the discrete scattering operator.

After convergence of source iteration (Experiment 6.5), we obtain the discrete-ordinates solution ψ^Q and compute the associated dose field \mathcal{D}^Q (as defined in the dose subsection preceding Experiment 6.4). To highlight the effect of angular scattering, Figure 9 places a number of choices of Henyey–Greenstein parameters. The dose exhibits increased lateral spread for smaller γ , reflecting redistribution of fluence away from purely characteristic transport directions.

6.7. Experiment 4: Angular discretisation study (ordinates and cone truncation). This experiment quantifies the effect of the angular approximation on the computed proton dose field. In the notation of Section 4, the angular approximation has two distinct components: the number of discrete ordinates Q (angular resolution) and, when the angular domain is restricted, the cone half-angle θ_c (truncation). We

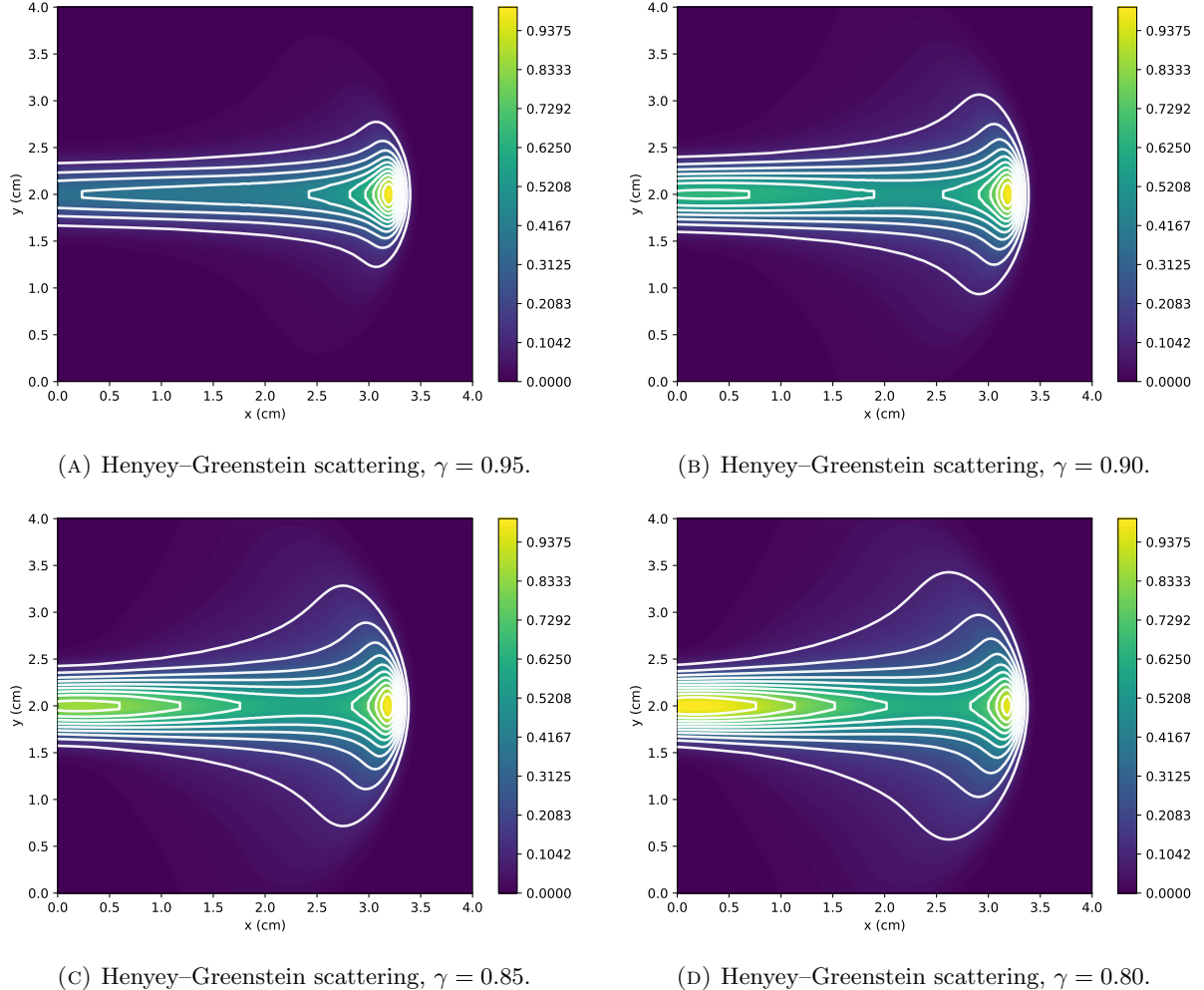


FIGURE 9. Dose fields D^Q computed with Henyey-Greenstein scattering (43) for $\gamma \in \{0.95, 0.90, 0.85, 0.80\}$. Decreasing γ induces visible lateral broadening of the beam relative to the more forward-peaked cases.

therefore study both effects within a single test configuration, with all other discretisation parameters held fixed.

We fix the spatial mesh, the energy grid and the stopping power $S(E)$ as in the preceding experiments. We model elastic scattering with the Henyey-Greenstein phase function (43) at a representative forward-peaked parameter $\gamma = 0.9$. For each angular discretisation, we run source iteration to a sufficiently tight tolerance so that the residual effect of iteration is negligible compared to angular discretisation effects (this is validated a posteriori using the successive-iterate diagnostic from Experiment 6.5).

To isolate the influence of Q and θ_c we compare against a numerically converged angular reference. Concretely, we compute a full-sphere discrete-ordinates reference solution $\psi^{Q_{\text{ref}}}$ with a large number of directions Q_{ref} , and define the corresponding reference dose $D^{Q_{\text{ref}}}$. For cone-restricted runs, we also consider a cone-reference at the same θ_c but with a large Q , denoted $D^{Q_{\text{ref}}, \theta_c}$, to distinguish cone truncation effects from pure quadrature resolution effects.

For any run with Q directions and cone half-angle θ_c we compute the dose field D^{Q,θ_c} (as defined in the dose subsection preceding Experiment 6.4) and report the relative dose error against the chosen reference

$$\mathcal{E}_\infty(Q, \theta_c) := \frac{\|D^{Q,\theta_c} - D^{\text{ref}}\|_{L^\infty(D)}}{\|D^{\text{ref}}\|_{L^\infty(D)}}, \quad D^{\text{ref}} \in \{D^{Q_{\text{ref}}}, D^{Q_{\text{ref}}, \theta_c}\}.$$

We additionally report a simple lateral-spread diagnostic at a fixed depth $x = x_\dagger$ (chosen in the mid-range of the track), defined as a second-moment beam width

$$W^{Q,\theta_c}(x_\dagger) := \left(\frac{\int_y (y - \bar{y})^2 D^{Q,\theta_c}(x_\dagger, y) dy}{\int_y D^{Q,\theta_c}(x_\dagger, y) dy} \right)^{1/2}, \quad \bar{y} := \frac{\int_y y D^{Q,\theta_c}(x_\dagger, y) dy}{\int_y D^{Q,\theta_c}(x_\dagger, y) dy},$$

which is stable under mesh refinement and directly reflects the scattering-induced lateral broadening.

To separate cone truncation effects from angular-resolution effects we use two distinct angular references. First, we compute a high-resolution maximal-cone reference dose $D^{Q_{\text{ref}}, \theta_{\max}}$, where θ_{\max} denotes the maximal cone used in the implementation (in the present 2D setting $\theta_{\max} = \pi/2$, that is, all forward directions). This reference serves as a proxy for the untruncated forward-direction model.

Second, for each cone half-angle θ_c in the sweep we compute a high-resolution cone reference $D^{Q_{\text{ref}}, \theta_c}$ on the same truncated angular domain. Comparing against $D^{Q_{\text{ref}}, \theta_c}$ therefore isolates the angular-resolution error inside the cone, since both solutions neglect out-of-cone scattering in exactly the same way.

Two parameter sweeps are performed.

- (1) Ordinates study. We fix the cone half-angle at its maximal value used in the implementation, denoted θ_{\max} . In the present 2D setting this corresponds to $\theta_{\max} = \pi/2$, that is, all forward directions. We then vary the number of discrete ordinates Q and compare the resulting dose fields $D^{Q,\theta_{\max}}$ against the maximal-cone reference $D^{Q_{\text{ref}}, \theta_{\max}}$ (here $Q_{\text{ref}} = 257$). We report the relative peak-normalised dose error $\mathcal{E}_\infty(Q, \theta_{\max})$ and the beam-width diagnostic $W^{Q,\theta_{\max}}(x_\dagger)$ defined above.
- (2) Cone-truncation study. We fix the angular resolution at $Q = Q_*$ (here $Q_* = 33$) and vary the cone half-angle $\theta_c \in \{\theta_{c,1}, \dots, \theta_{\max}\}$. For each θ_c we report two errors: $\mathcal{E}_\infty(Q_*, \theta_c)$ measured against the maximal-cone reference $D^{Q_{\text{ref}}, \theta_{\max}}$ (capturing the combined effect of cone truncation and angular resolution) and the corresponding error measured against the cone reference $D^{Q_{\text{ref}}, \theta_c}$ (isolating the angular-resolution effect inside the truncated cone), with $Q_{\text{ref}} = 129$ for this sweep. Note that, with Q_* fixed, enlarging the cone simultaneously decreases truncation error and coarsens the angular partition, so the error against $D^{Q_{\text{ref}}, \theta_{\max}}$ reflects a trade-off between truncation and resolution and need not be monotone in θ_c .

Figure 10 collects the two error curves, one for ordinates refinement and one for cone truncation. Figure 11 shows the stabilisation of the beam-width diagnostic under ordinates refinement. Finally, Figure 12 provides representative dose snapshots for four cone half-angles, illustrating the qualitative impact of truncation.

6.8. Experiment 5: Coupling through scattering and iteration behaviour. This experiment assesses the practical coupling strength induced by elastic scattering in the discrete-ordinates system and its impact on the convergence of source iteration. The analysis in Section 5.6 predicts linear convergence under a subcriticality condition, with slower contraction as the effective scattering strength increases. Here we verify this behaviour in a physically meaningful regime.

We fix the spatial mesh, energy grid, stopping power $S(E)$ and angular discretisation (either full sphere at a chosen Q or a cone with prescribed θ_c) as in Experiment 6.7. We consider a family of Henyey–Greenstein parameters $\gamma \in (0, 1)$, spanning moderately anisotropic to strongly forward-peaked scattering. For each γ we run the source iteration scheme to a fixed tolerance TOL and record both the successive-iterate diagnostic and the iteration count.

Let $\psi^{Q,n} = (\psi_1^{Q,n}, \dots, \psi_Q^{Q,n})$ denote the n th iterate of the angularly discrete system, where each $\psi_i^{Q,n}(\mathbf{x}, E)$ is obtained by one method-of-characteristics sweep in direction ω_i with a right-hand side assembled from $\psi^{Q,n-1}$. To quantify convergence we monitor the maximum successive-iterate difference

$$(44) \quad \Delta_\infty^{(n)} := \max_{1 \leq i \leq Q} \|\psi_i^{Q,n} - \psi_i^{Q,n-1}\|_{L^\infty(D \times I)}.$$

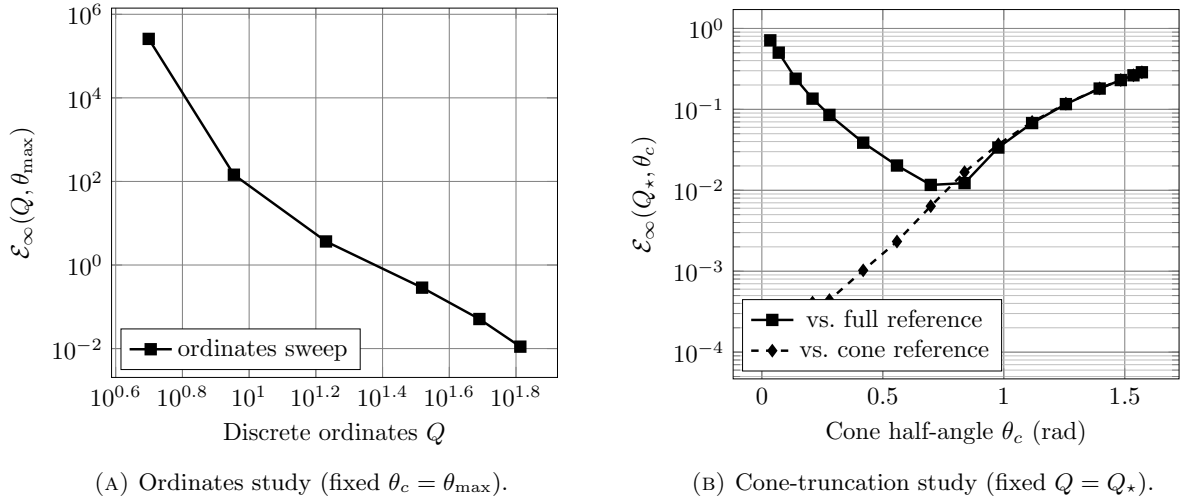


FIGURE 10. Angular discretisation error study with Henyey–Greenstein scattering at $\gamma = 0.9$. Left: convergence of the dose error under ordinates refinement at fixed $\theta_c = \theta_{\max}$. Right: error versus cone half-angle at fixed $Q = Q_*$. The curve shown against the maximal-cone reference captures both cone truncation and angular-resolution effects, while the curve shown against the cone reference isolates the angular-resolution effect inside the truncated cone.

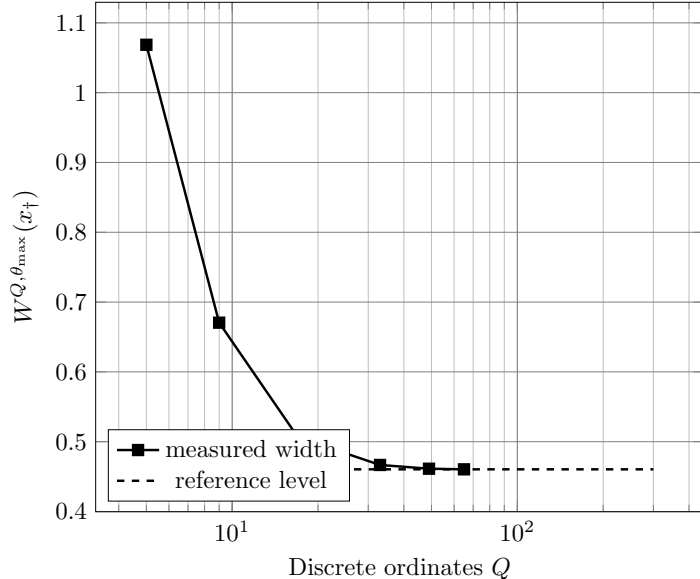


FIGURE 11. Beam-width diagnostic under ordinates refinement (Henyey–Greenstein, $\gamma = 0.9$), shown at the fixed depth $x = x_f$. The dashed line indicates the value obtained at the finest ordinates level in the sweep.

This quantity is inexpensive to compute, is directly available from the stored iterates and serves as a practical stopping proxy for the a posteriori bound in Section 5.6. We also report the iteration count $n_{\text{it}}(\gamma)$ required to achieve $\Delta_\infty^{(n)} \leq \text{TOL}$.

We present two figures. Figure 14 compares the decay of $\Delta_\infty^{(n)}$ for several values of γ , demonstrating that the iteration contracts more slowly as scattering becomes more strongly forward-peaked and hence

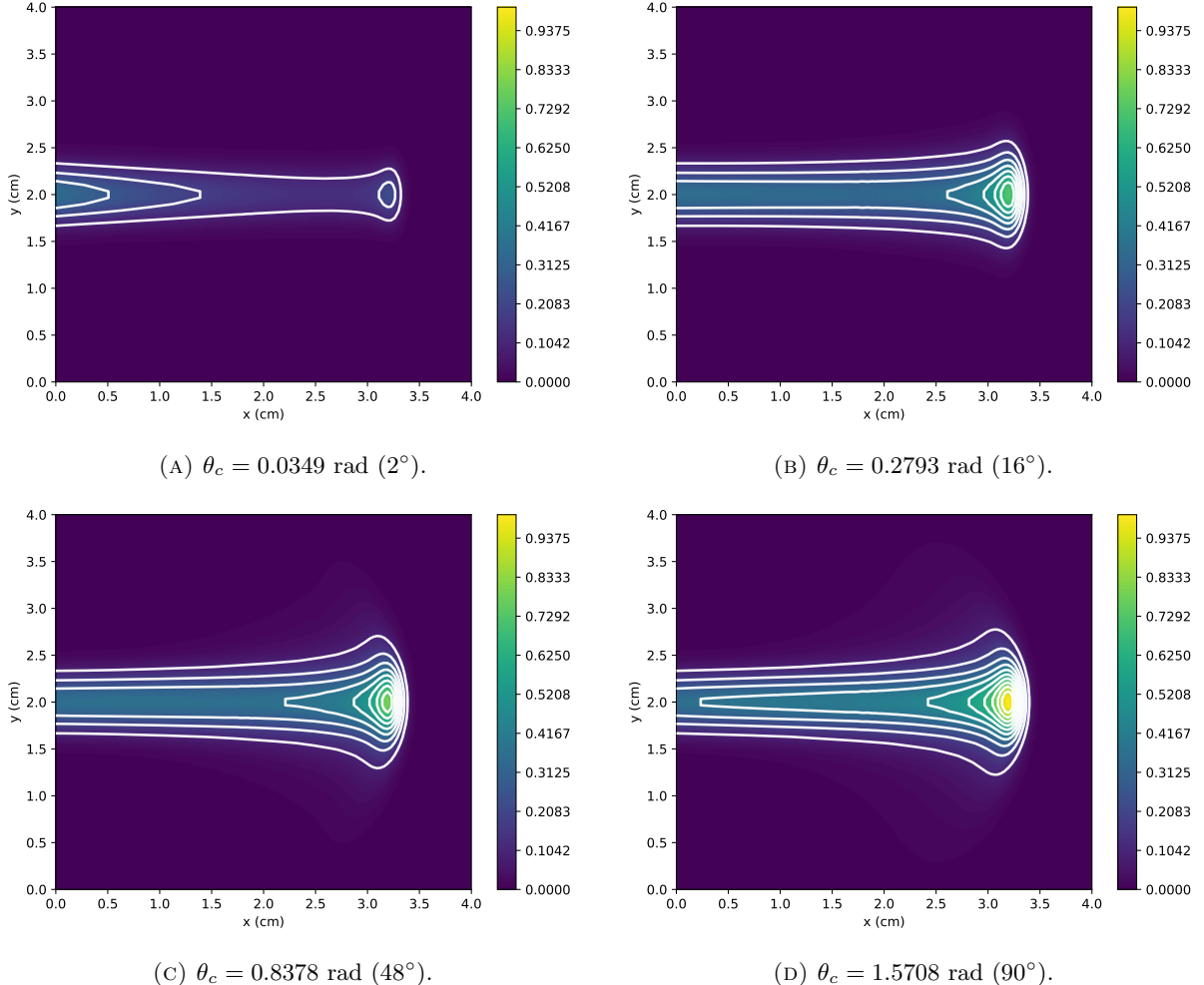


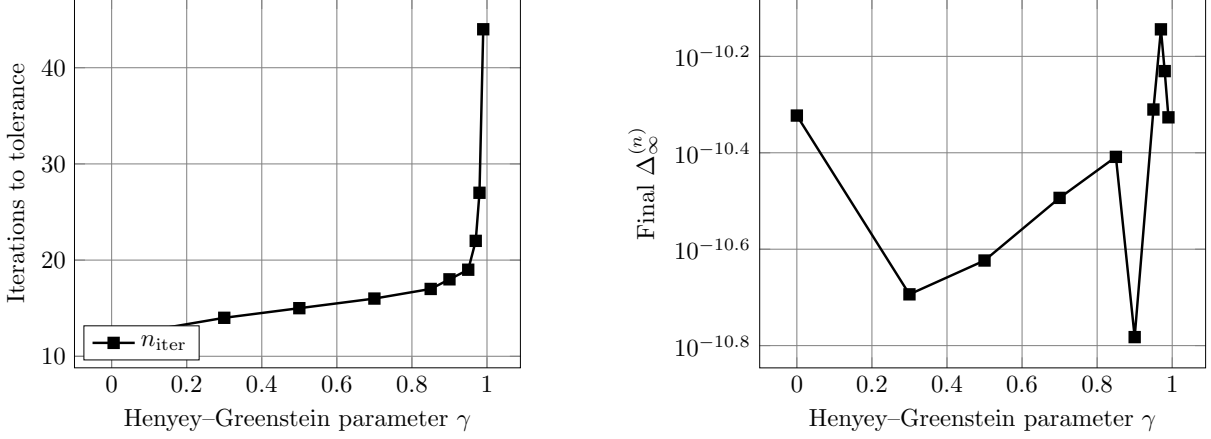
FIGURE 12. Representative dose fields D^{Q_*, θ_c} from the cone-truncation sweep (Henyey–Greenstein, $\gamma = 0.9$, fixed $Q = Q_*$), illustrating how overly small cones under-represent wide-angle scattering and suppress lateral spread.

more redistributive within the discretised angular domain. Figure 13 reports the iteration count $n_{\text{it}}(\gamma)$ as a function of γ .

7. NUMERICAL EXPERIMENTS: CARBON ION TRANSPORT

Unlike protons, carbon ions undergo nuclear interactions and fragmentation in water, producing a broad spectrum of secondary particles. The goal of this section is a demonstration of a multi-species workflow built on the same characteristic sweeping infrastructure as the proton solver. A scattered carbon primary field is computed first, then secondary protons and neutrons are generated from the converged carbon solution through prescribed volumetric sources and transported in reduced models. Our emphasis is out-of-field exposure, so we focus on neutrons (long-range transport and relevance to protection quantities) and include secondary protons as a simple charged-fragment proxy.

7.1. Experiment 6: Out-of-field secondaries in carbon transport (protons and neutrons). Carbon primaries are transported with continuous slowing down driven by a tabulated stopping power. Let $S_C(E)$ denote the linear stopping power (MeV/cm) for carbon ions in water expressed in terms of the total ion energy E (MeV). As in the proton experiments, we work with an angularly discrete representation and



(a) Source-iteration counts vs. anisotropy parameter γ . (b) Final successive-iterate diagnostic at termination.

FIGURE 13. Dependence of source-iteration performance on the scattering anisotropy parameter γ .

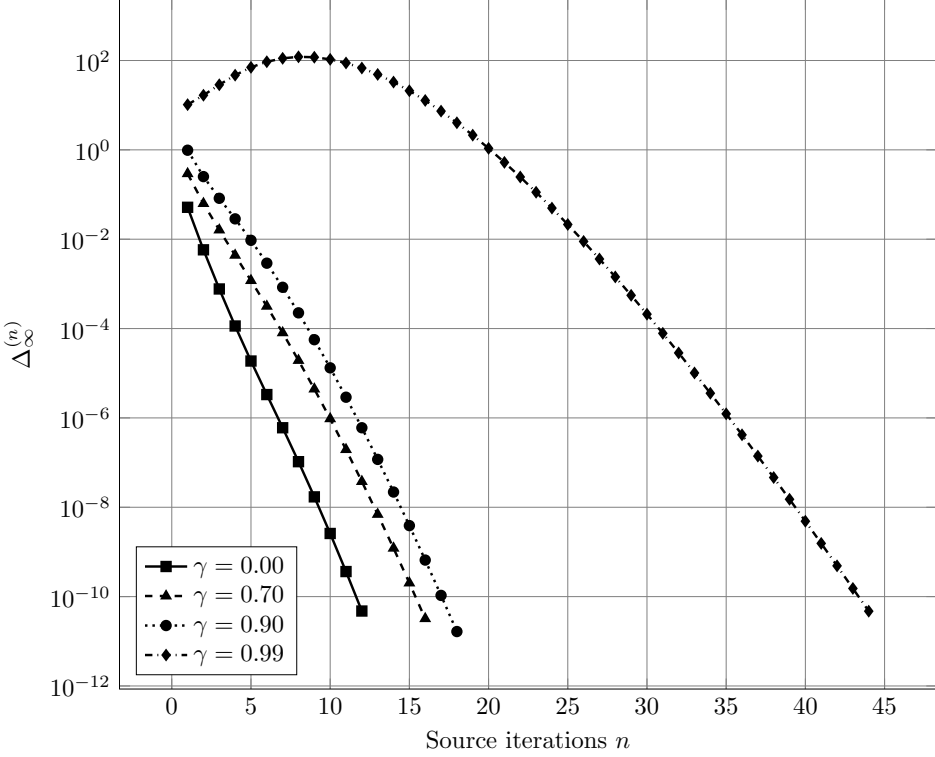


FIGURE 14. Convergence histories $\Delta_\infty^{(n)} = \max_{1 \leq i \leq Q} \|\psi_i^{Q,n} - \psi_i^{Q,n-1}\|_{L^\infty(D \times I)}$ for representative Henyey-Greenstein parameters γ .

compute directional carbon fluence $\Psi_i^C : D \times I \rightarrow \mathbb{R}$, $i = 1, \dots, Q$, from

$$(45) \quad \boldsymbol{\omega}_i \cdot \nabla_{\mathbf{x}} \Psi_i^C(\mathbf{x}, E) - \partial_E (S_C(E) \Psi_i^C(\mathbf{x}, E)) + \sigma_T^C(E) \Psi_i^C(\mathbf{x}, E) = \sum_{j=1}^Q \mu_j \bar{\sigma}_{\text{el}}^C(\boldsymbol{\omega}_i, \boldsymbol{\omega}_j) \Psi_j^C(\mathbf{x}, E),$$

supplemented by a forward inflow carbon beam (supported only in the central angular node, with the remaining inflow bins set to zero). The right-hand side is treated by source iteration, with each iteration step consisting of Q independent method-of-characteristics sweeps. The characteristic map required by the sweep is defined using a fitted Bragg–Kleeman range law $R_{\text{BK}}(E) = \alpha_C E^{p_C}$, while all dose postprocessing uses the tabulated $S_C(E)$.

From the converged carbon solution we form the scalar carbon fluence and dose

$$(46) \quad \Phi^C(\mathbf{x}, E) := \sum_{i=1}^Q \varpi_i \Psi_i^C(\mathbf{x}, E), \quad D_C^Q(\mathbf{x}) := \int_I S_C(E) \Phi^C(\mathbf{x}, E) \, dE.$$

To drive secondaries we introduce an effective macroscopic nuclear interaction rate $\Sigma_{\text{nuc}}(E)$ and define the interaction proxy

$$(47) \quad \mathcal{I}^C(\mathbf{x}) := \int_I \Sigma_{\text{nuc}}(E) \Phi^C(\mathbf{x}, E) \, dE,$$

which concentrates secondary production in regions of high primary fluence and high interaction probability. Secondary protons and neutrons are then generated by volumetric sources that factorise into a spatial production rate $\mathcal{I}^C(\mathbf{x})$, an emitted-energy density and a simple angular distribution. Concretely, we take

$$(48) \quad Q_i^P(\mathbf{x}, E_P) = Y_P \mathcal{I}^C(\mathbf{x}) w_P(E_P) \frac{1}{Q}, \quad Q_i^N(\mathbf{x}, E_N) = Y_N \mathcal{I}^C(\mathbf{x}) w_N(E_N) \frac{1}{Q},$$

where Y_P and Y_N are yield parameters, while w_P and w_N are prescribed energy densities. The uniform $1/Q$ factor corresponds to an isotropic redistribution over the discrete ordinates; this can be replaced by a forward-peaked emission model or by a data-driven angular distribution without changing the solver structure.

Given the sources, secondary protons are transported with ionisation loss only,

$$(49) \quad \boldsymbol{\omega}_i \cdot \nabla_{\mathbf{x}} \Psi_i^P(\mathbf{x}, E_P) - \partial_{E_P} (S_P(E_P) \Psi_i^P(\mathbf{x}, E_P)) = Q_i^P(\mathbf{x}, E_P),$$

with no inflow contribution, while neutrons are propagated in a reduced streaming–removal model with no energy loss term,

$$(50) \quad \boldsymbol{\omega}_i \cdot \nabla_{\mathbf{x}} \Psi_i^N(\mathbf{x}, E_N) + \sigma_T^N(E_N) \Psi_i^N(\mathbf{x}, E_N) = Q_i^N(\mathbf{x}, E_N),$$

again with no inflow contribution. The associated secondary doses are computed from the scalar secondary fluences $\Phi^P = \sum_{i=1}^Q \varpi_i \Psi_i^P$ and $\Phi^N = \sum_{i=1}^Q \varpi_i \Psi_i^N$ as

$$(51) \quad D_P(\mathbf{x}) := \int_{I_P} S_P(E_P) \Phi^P(\mathbf{x}, E_P) \, dE_P, \quad D_N(\mathbf{x}) := \int_{I_N} \kappa_N(E_N) \Phi^N(\mathbf{x}, E_N) \, dE_N,$$

where κ_N is a prescribed kerma coefficient. The total dose is $D(\mathbf{x}) := D_C^Q(\mathbf{x}) + D_P(\mathbf{x}) + D_N(\mathbf{x})$.

Figure 15 shows the spatial dose components for a representative configuration. The carbon primary dose D_C^Q exhibits a pronounced Bragg peak localised near the calibrated range. The forced secondary proton dose D_P is smoother in depth and typically produces a distal tail beyond the primary peak due to the volumetric nature of the source and the broad emitted energy spectrum. The neutron kerma dose D_N forms a low-amplitude halo extending away from the production region under ballistic transport with removal. The sum D illustrates how even a reduced multi-species construction can generate post-peak and out-of-field dose structure beyond a purely primary CSDA model.

To make the distal and out-of-field behaviour easier to interpret, Figure 16 plots central depth–dose curves extracted from a narrow band about the mid-plane, using the same diagnostic averaging as in the proton experiments. The carbon curve shows primary peak localisation, while the secondary proton contribution provides a smooth continuation past the peak. The neutron kerma component remains small in-field but extends further downstream and laterally, consistent with the streaming–removal model.

7.2. Remark (Scope of secondaries and follow-on modelling). *Carbon–water nuclear interactions generate many secondary species. The present experiment is intentionally reduced. It is motivated by out-of-field endpoints, we retain neutrons as the principal long-range component and include secondary protons as a simple charged-fragment proxy. The source construction (48) is designed to be replaced by data-driven yields*

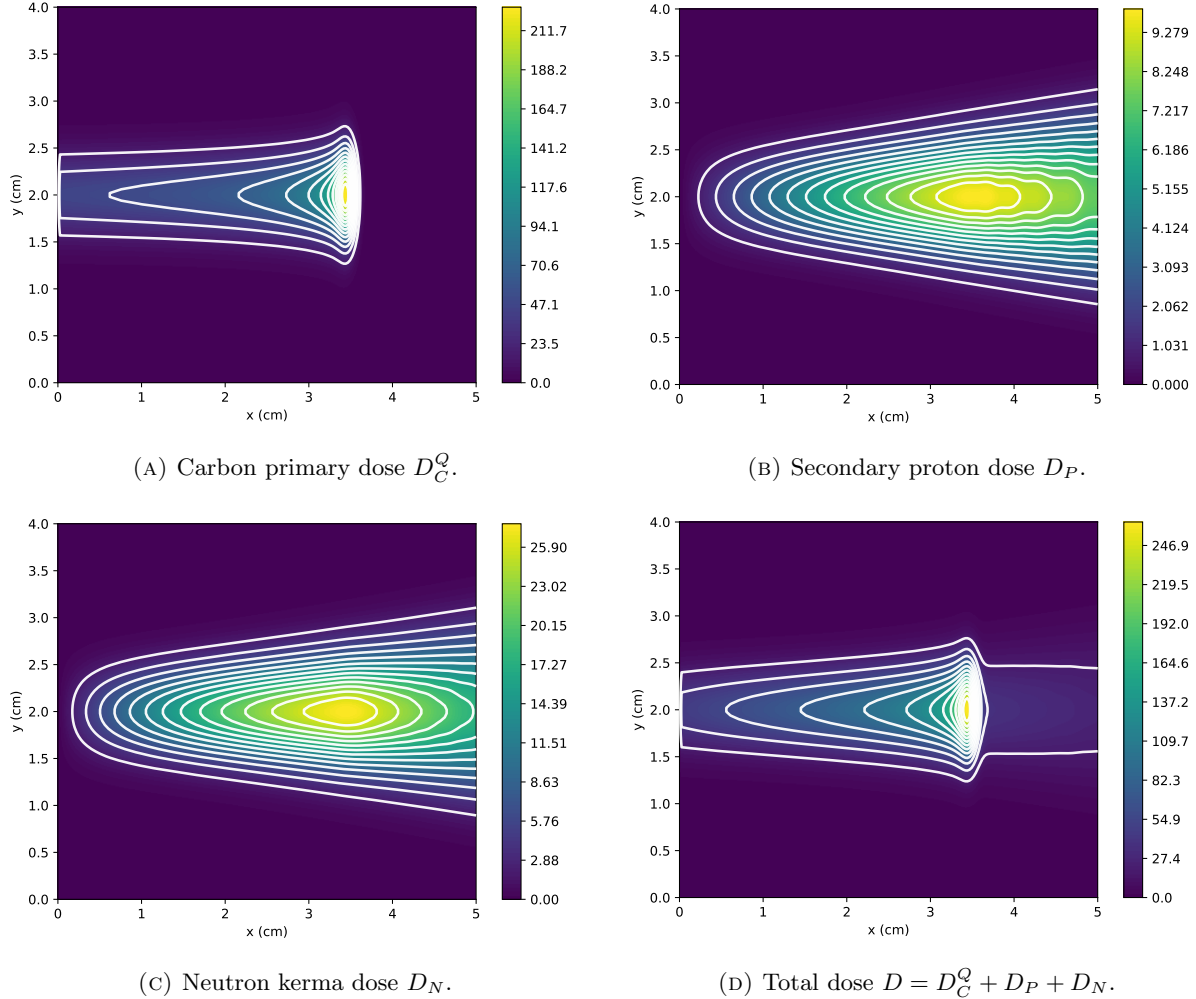


FIGURE 15. Multi-species carbon example. Dose components computed from a scattered carbon primary field together with forced secondary proton and neutron solves driven by the interaction proxy \mathcal{I}^C . The secondary components are displayed on the same spatial domain to highlight formation of a distal tail and a low-dose halo beyond the primary carbon Bragg peak.

and emitted spectra and extended to additional fragment species and protection quantities without changing the transport solvers or postprocessing. This is developed further in the follow-on study [5].

ACKNOWLEDGEMENTS

This work was initiated at a workshop hosted by Mathrad, supported by the EPSRC programme grant EP/W026899/1, which subsequently funded TP. BA and TP also received support from the Leverhulme Trust grant RPG-2021-238 and TP the EPSRC grant EP/X030067/1. The research was conducted by a working group sponsored by the radioprotection theme of the Institute for Mathematical Innovation partially funding BA.

REFERENCES

[1] M. L. Adams and E. W. Larsen. “Fast iterative methods for discrete-ordinates particle transport calculations”. In: *Progress in nuclear energy* 40.1 (2002), pp. 3–159.

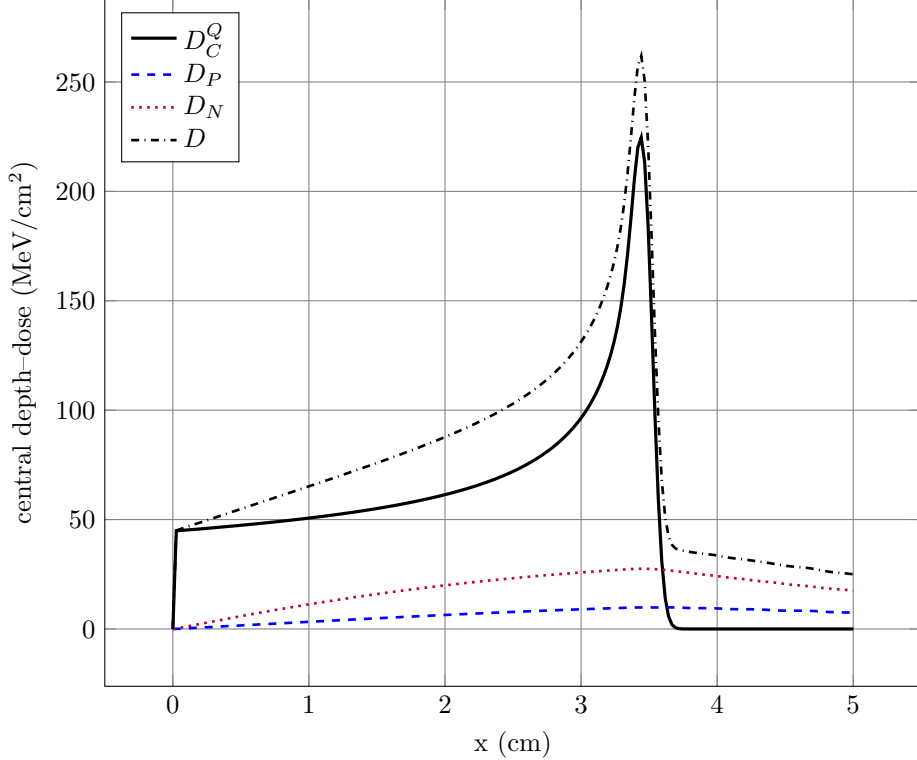


FIGURE 16. Central depth-dose curves for the carbon primary dose D_C^Q , secondary proton dose D_P , neutron kerma dose D_N and total dose $D = D_C^Q + D_P + D_N$, extracted by averaging over a narrow band about the mid-plane. The secondary proton component produces a smooth distal tail beyond the primary carbon peak, while the neutron component extends further under ballistic transport with removal and is therefore relevant for out-of-field exposure.

- [2] S. Agostinelli et al. “Geant4—a simulation toolkit”. In: *Nuclear instruments and methods in physics research section A: Accelerators, Spectrometers, Detectors and Associated Equipment* 506.3 (2003), pp. 250–303.
- [3] B. S. Ashby, A. Hamdan, and T. Prys. “A Positivity-Preserving Finite Element Framework for Accurate Dose Computation in Proton Therapy”. In: *arXiv preprint arXiv:2506.01105* (2025).
- [4] B. S. Ashby et al. “Efficient proton transport modelling for proton beam therapy and biological quantification”. In: *Journal of Mathematical Biology* 90.5 (2025), pp. 1–33.
- [5] B. S. Ashby, T. Prys, and M. Southerby. “A Multispecies Transport Surrogate for Out-of-Field Dose and Protection Quantities in Ion-Beam Therapy”. In: *Preprint* (2026).
- [6] M. J. Berger et al. *ESTAR, PSTAR, and ASTAR: Computer Programs for Calculating Stopping-Power and Range Tables for Electrons, Protons, and Helium Ions (version 1.2.3)*. National Institute of Standards and Technology, Gaithersburg, MD. [Online; accessed 2025-12-29]. 2005.
- [7] M. J. Berger and S. M. Seltzer. “Stopping powers and ranges of electrons and positrons”. In: *Unknown* (1982).
- [8] M. J. Berger et al. *Stopping-power and range tables for electrons, protons, and helium ions*. NIST Physics Laboratory Gaithersburg, MD, 1998.
- [9] C. Börgers and E. W. Larsen. “On the accuracy of the Fokker–Planck and Fermi pencil beam equations for charged particle transport”. In: *Medical Physics* 23.10 (1996), pp. 1749–1759.
- [10] A. Calloo et al. “Cycle-free polytopal mesh sweeping for Boltzmann transport”. In: *Numerical Algorithms* (2025), pp. 1–24.

[11] K. M. Case, P. F. Zweifel, and G. Pomraning. *Linear transport theory*. 1968.

[12] M. Cessenat. “Théoremes de trace L^p pour des espaces de fonctions de la neutronique”. In: *Comptes rendus des séances de l'Académie des sciences. Série 1, Mathématique* 299.16 (1984), pp. 831–834.

[13] M. Cessenat and R. DAUTRAY. “Théoremes de trace pour des espaces de fonctions de la neutronique”. In: *Comptes rendus des séances de l'Académie des sciences. Série 1, Mathématique* 300.3 (1985), pp. 89–92.

[14] V. Chronholm and T. Prys. “Geometry, energy and sensitivity in stochastic proton dynamics”. In: *arXiv preprint arXiv:2509.13223* (2025).

[15] A. M. Cox et al. “A Bayesian inverse approach to proton therapy dose delivery verification”. In: *Proceedings A*. Vol. 480. 2301. The Royal Society. 2024, p. 20230836.

[16] A. Crossley et al. “Jump stochastic differential equations for the characterization of the Bragg peak in proton beam radiotherapy”. In: *Proceedings of the Royal Society A* 481.2310 (2025), p. 20240687.

[17] C. B. Dean et al. “Fast SDE-based Monte Carlo dose calculation for proton therapy validated against Geant4”. In: *arXiv preprint arXiv:2511.03115* (2025).

[18] M. Evans and T. Prys. “Reyna: A minimal overhead polytopal discontinuous Galerkin finite element library”. In: *Journal of Open Source Software* 11.118 (2026), p. 9292. DOI: [10.21105/joss.09292](https://doi.org/10.21105/joss.09292).

[19] M. Fippel and M. Soukup. “A Monte Carlo dose calculation algorithm for proton therapy”. In: *Medical physics* 31.8 (2004), pp. 2263–2273.

[20] T. Goorley et al. “Initial MCNP6 release overview”. In: *Nuclear technology* 180.3 (2012), pp. 298–315.

[21] L. G. Henyey and J. L. Greenstein. “Diffuse radiation in the galaxy”. In: *Astrophysical Journal, vol. 93, p. 70-83 (1941)*. 93 (1941), pp. 70–83.

[22] L. Hong et al. “A pencil beam algorithm for proton dose calculations”. In: *Physics in Medicine & Biology* 41.8 (1996), p. 1305.

[23] P. Houston, M. E. Hubbard, and T. J. Radley. “Iterative solution methods for high-order/hp–DGFEM approximation of the linear Boltzmann transport equation”. In: *Computers & Mathematics with Applications* 166 (2024), pp. 37–49.

[24] P. Houston et al. “Efficient high-order space-angle-energy polytopic discontinuous Galerkin finite element methods for linear Boltzmann transport”. In: *Journal of Scientific Computing* 100.2 (2024), p. 52.

[25] International Commission on Radiation Units and Measurements. “Stopping of Ions Heavier Than Helium”. In: *Journal of the ICRU* 5.1 (2005). DOI: [10.1093/jicru/ndi002](https://doi.org/10.1093/jicru/ndi002).

[26] M. W. Kan, P. K. Yu, and L. H. Leung. “A review on the use of grid-based Boltzmann equation solvers for dose calculation in external photon beam treatment planning”. In: *BioMed Research International* 2013.1 (2013), p. 692874.

[27] A. E. Kyprianou, A. Pim, and T. Prys. “A Unified Framework from Boltzmann Transport to Proton Treatment Planning”. In: *arXiv preprint arXiv:2508.10596* (2025).

[28] E. E. Lewis and W. F. Miller. “Computational methods of neutron transport”. In: (1984).

[29] I. Lux. *Monte Carlo particle transport methods*. CRC press, 2018.

[30] D. S. Miller, G. Rodrigue, and F. Graziani. “A convergence analysis of source iteration for the solution of coupled transport equations on a stochastic media”. In: (2002).

[31] A. Pim and T. Prys. “Surrogate Modelling of Proton Dose with Monte Carlo Dropout Uncertainty Quantification”. In: *arXiv preprint arXiv:2509.18155* (2025).

[32] G. C. Pomraning. *Linear kinetic theory and particle transport in stochastic mixtures*. Vol. 7. World Scientific, 1991.

[33] I. C. on Radiation Units and Measurements. *Stopping powers and ranges for protons and alpha particles*. International commission on radiation units and measurements, 1993.

[34] S. Seltzer et al. “Key data for ionizing-radiation dosimetry: measurement standards and applications, ICRU Report 90”. In: (2016).

[35] P. Sigmund, A. Schinner, and H. Paul. “Errata and addenda for ICRU report 73, stopping of ions heavier than helium”. In: *J ICRU* 5.1 (2009), pp. 1–10.

[36] P. Stammer et al. “A Deterministic Dynamical Low-rank Approach for Charged Particle Transport”. In: *arXiv preprint arXiv:2412.09484* (2024).

- [37] J. W. Wilson et al. “Charged-particle transport in one dimension”. In: *Nuclear Science and Engineering* 99.3 (1988), pp. 285–287.
- [38] Y. Yu et al. “Review of the Discrete-Ordinates Method for Particle Transport in Nuclear Energy”. In: *Energies* 18.11 (2025), p. 2880.

¹ INSTITUTE FOR MATHEMATICAL INNOVATION, UNIVERSITY OF BATH, BATH, UK. ² DEPARTMENT OF MATHEMATICAL SCIENCES, UNIVERSITY OF BATH, BATH, UK. ³ DEPARTMENT OF MATHEMATICS AND STATISTICS, UNIVERSITY OF READING, READING, UK.